

First spaceborne observation of an Earth-reflected GPS signal

Stephen T. Lowe, John L. LaBrecque,¹ Cinzia Zuffada, Larry J. Romans, Larry E. Young, and George A. Hajj

Jet Propulsion Laboratory, California Institute of Technology, Pasadena, California, USA

Received 7 August 2000; revised 31 May 2001; accepted 7 September 2001; published 7 February 2002.

[1] We present the first spaceborne observation of a Global Positioning System (GPS) signal reflected from the Earth's surface, specifically from the Pacific Ocean. This result is scaled to obtain the expected voltage signal-to-noise ratio (SNR) and altimetric accuracy for a generic GPS reflections altimetry mission and the current SAC-C and CHAMP missions. Cross-correlating a three-parameter phase model with both a 1-s and 4-s segment of spaceborne imaging radar-C (SIR-C) calibration data, recorded before and after a Galapagos Islands imaging pass, results in beam-limited signals having voltage SNRs of 10 and 334, respectively. Evidence for these results being reflected GPS signals includes: (1) The signals' temporal shapes agree closely with that predicted using a detailed scattering model, at two different observation geometries, and differ significantly from the expected direct signal shapes. (2) The signal in the 4-s data has a measured coherence time of 1.0 ms, which agrees closely with that expected for a reflected signal and is completely inconsistent with the direct signal's coherence properties. (3) The 1- and 4-s signals' voltage SNR is maximized by shifting the model frequency -2740 Hz and 497 Hz, respectively from that expected from their respective specular reflection points, or -2875 Hz and 690 Hz from the expected direct signal frequencies. These values agree with the -2900 Hz and 510 Hz Doppler frequency shifts expected from those points on the surface corresponding to the antenna's pointing direction, thus illustrating beam-steering effects on the surface. (4) Plausible hypotheses for the detected waveform being a corrupted direct signal, including second-order mismodeling effects, shuttle multipath effects, or a band-pass cutoff of the GPS spread spectrum, are shown to be inconsistent with the data. Space-based observations of reflected GPS signals, like the ones presented here, may enable a new class of ocean topography measurements unavailable from traditional altimeters, such as TOPEX/Poseidon, and perhaps surface wind vector measurements. Making such observations with sufficient SNR will require unusually large, high-gain antennas. The measurement presented here is scaled to assess the expected SNR for those applications. Because this result lies in a nonlinear scaling regime, the correct scaling equations are presented, and the expected signal strength from a generic GPS reflections altimetry mission is derived to illustrate the most important contributions to the signal SNR. An SNR estimate is also derived for the SAC-C and CHAMP missions, which are expected to make GPS reflection measurements in the near future. Finally, a qualitative wind speed determination is extracted from the observed signal. *INDEX TERMS*: 0933 Exploration Geophysics: Remote sensing; 6959 Radio Science: Radio oceanography; *KEYWORDS*: GPS reflections, ocean altimetry

1. Introduction and Motivation

[2] A novel remote-sensing capability has been proposed [Martin-Neira, 1993] to observe the ocean utilizing

GPS signals scattered off its surface and sensed by an airborne or spaceborne receiver. With 24 GPS transmitters a single such receiver results in a multistatic system, capable of intercepting reflections from several simultaneous ocean regions. Figures 1a and 1b compare this geometry with the traditional monostatic radar geometry, used by missions such as TOPEX/Poseidon or Jason-1. Accurate measurements of the reflected signals, along with knowledge of the receiver and transmitter positions, can

¹Now at NASA, Washington, D. C., USA.

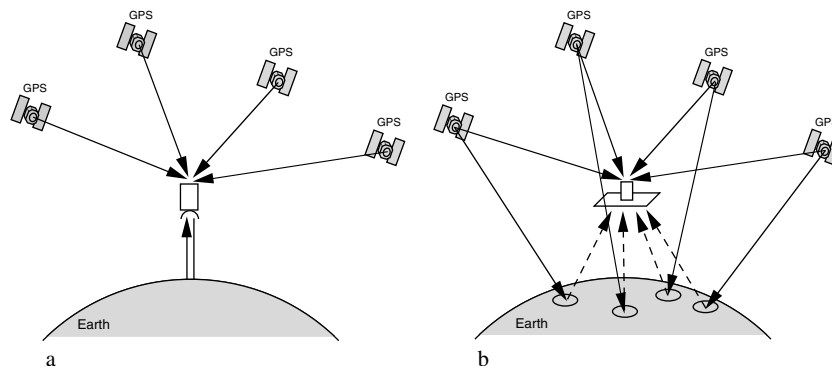


Figure 1. (a) A typical monostatic radar altimetry mission, such as TOPEX/Poseidon, where the radar transmitter and receiver are located by the GPS constellation and the ocean height at nadir is calculated from the radar's round-trip travel time. (b) A passive multistatic altimetry system created from several GPS satellites. The GPS constellation provides the receiver location, and the measured time difference between the direct and reflected signal arrival times determines the ocean height simultaneously at several specular points. A phased array antenna can provide simultaneous high gain for each incoming signal.

yield information on the ocean's height, roughness, and other parameters. GPS reflection measurements from low-Earth orbit have the potential to provide data for global mesoscale mapping, ocean wind speed and direction determinations, significant wave heights, ice mapping, and ice-sea interface studies, using relatively low cost, passive instrumentation. In pursuit of these capabilities, GPS reflections have been observed over the ocean from a variety of low-altitude (≤ 25 km) platforms, including bridges, airplanes, and balloons [Martin-Neira *et al.*, 2001; Garrison *et al.*, 1998; Komjathy *et al.*, 2000; Garrison, 1998], and over a variety of terrain, including lakes, wetlands, deserts, urban areas, and ice [Katzberg, 1998; Lowe *et al.*, 1998; A. Komjathy *et al.*, On the retrieval of sea ice information using GPS surface reflected measurements, submitted to *Remote Sensing of the Environment*, 2001], but no signals have been previously observed from space because of very weak signal strengths and rare observational opportunities.

[3] One specific science application of GPS reflection measurements is the study of ocean eddies. To understand global climate change, it is essential to know the amount of heat the oceans and atmosphere are carrying, and eddies play an important role in current dynamics and in global heat transport. Eddies are like the "storms" of the ocean and extract energy from the upper, wind-driven layers of circulation and transfer it to greater depths. Existing ocean models, including those used for climate forecasting, are far from properly resolving ocean eddies, and therefore the uncertainties associated with the model predictions remain undetermined. Because eddies are typically only a few hundred kilometers across and can travel on the order

of 100 km d^{-1} , the 10-day repeat cycle and 300-km cross-track spacing of TOPEX/Poseidon make it impossible to observe and track individual eddies. The dense coverage of GPS reflections, both temporally and spatially, might enable monitoring of ocean eddies and therefore provide a unique measurement capability. An important step in assessing this technology is to observe reflected signals from space and characterize them as a function of geometric and oceanographic parameters. The signal strength and temporal signature can then be compared to, and help strengthen, GPS reflection models currently under development using low-altitude observations.

[4] Section 2 discusses our search for existing data sets that could potentially contain reflected GPS signals, and the resulting SIR-C data set. Section 3 covers the signal search in detail, including a derivation of our model and techniques used to perform the search efficiently, along with the resulting measured signal. Section 4 presents evidence that the two signals found are indeed reflected by comparing the signals' temporal shape, coherence properties, and reception frequency with that expected for both direct and reflected signals. Section 5 covers how this signal might be interpreted, including scaling to a generic ocean altimetry mission, SAC-C and CHAMP and a qualitative wind speed determination.

2. Data Set Survey

2.1. Data Selection

[5] The large potential benefit from spaceborne GPS reflection measurements, combined with a lack of obser-

ational opportunities, motivated a search for existing data sets which might fortuitously contain GPS reflection signals. The first selection criterion was that the data must have been collected using a high-gain antenna to enhance the very weak reflected signal. To formulate the second criterion, one must consider the following facts concerning the GPS signal structure: (1) The two GPS L-band navigation signals, L1 and L2, have carrier frequencies of 1575.42 MHz and 1227.6 MHz, respectively. (2) Both L1 and L2 are modulated with pseudorandom noise (PRN) codes which randomly either change the carrier phase by 180° or leave it unchanged. The intervals between possible phase changes are called chips, to distinguish them from information-containing bits. (3) Each GPS satellite transmitter is assigned a unique PRN and identification number. (4) The L1 signal is modulated with both the public C/A code and the classified Y code, having 1.023-MHz and 10.23-MHz chip frequencies, respectively. The L2 signal is only modulated with the classified Y code. (5) Both L1 and L2 are additionally modulated by the navigation data message, having a 50-Hz bit rate. (6) The PRN chips have the effect of spreading the carrier frequency power into a sinc-squared function centered at the carrier frequency with the first null at the carrier plus/minus the chip frequency.

[6] The second data selection criterion was that the receiver's passband contain either the GPS L1 or L2 PRN spread spectrum (1565.42–1585.42 MHz or 1217.60–1237.60 MHz). Finally, we required data recorded over an ocean, as the high conductivity and relatively flat surface, compared to typical land topography, would maximize the reflected signal strength. These three criteria lead to the spaceborne imaging radar-C (SIR-C) experiment on board the Space Radar Laboratory 2 (SRL 2) mission that flew in October 1994. This experiment used a large, 38-dB, linear-polarized antenna on board the shuttle to collect reflected radar signals for mapping purposes, and the recording band pass contained most of the L2 spread spectrum, but no L1 signal. Having only the L2 signal required our obtaining the Y code sequence transmitted during the data track for the data analysis effort. (The algorithm that generates the Y code is classified, but the actual transmitted Y code sequence is unclassified 0.1 s after transmission.)

2.2. SIR-C Data Set

[7] A typical SIR-C data track consisted of the receiver turning on and recording a few seconds of

noise for calibrations, followed by the radar turning on for a few minutes of imaging. After imaging, the radar was turned off while the recorder remained on, to again collect a few seconds of calibration noise data before ending the track. Our search was constrained to the receive-only calibration data at the track ends because it was assumed, and later confirmed, that the active radar would significantly increase the effective system noise, making GPS signal detection practically impossible. Our search was also confined to data taken in a "high-resolution" mode that had the GPS L2 signal and some Global Navigation Satellite System (GLO-NASS) (a Russian navigation system similar to GPS) signals in its passband.

[8] Because these data were collected for radar imaging, it was considered unlikely that a candidate data set having a favorable geometry for GPS reflections would be found. Most data were taken over land, where the reflected signal is much weaker than over the ocean, only a few seconds of high-resolution, radar-off calibration data were recorded per track, and it was considered unlikely that the antenna would fortuitously point toward a GPS specular reflection point. Despite the low probability of success a search was performed on SIR-C data abstracts to determine if any data had a favorable geometry. A geometric model was created using the shuttle and GPS satellite positions and the SIR-C antenna's pointing position on the Earth's surface. The specular reflection points for all GPS satellites were calculated and compared with the antenna pointing positions at the beginning and end of all high-resolution tracks. In spite of the fact that only one track, an imaging pass over the Galapagos Islands, was found to have a favorable geometry, this track appeared especially fortuitous. Figure 2 shows the shuttle track, and the tracks of the GPS specular points. The specular reflection point corresponding to GPS 39, with PRN 9, was found to be very close to the radar mapping region for the entire track. With such a favorable possibility we requested and obtained the raw data for this track from the SIR-C archives and began a search for the reflected GPS signal.

[9] Figure 3a illustrates the geometry of the Galapagos Islands 4-s data set with some specific distances and angles. The figure shows a vector, normal to the Earth's surface, at the specular reflection point (the reflection point assuming no surface roughness). The ellipse centered on the specular reflection point represents those points whose reflected signal arrives simultaneously at the receiver a given time later than that from

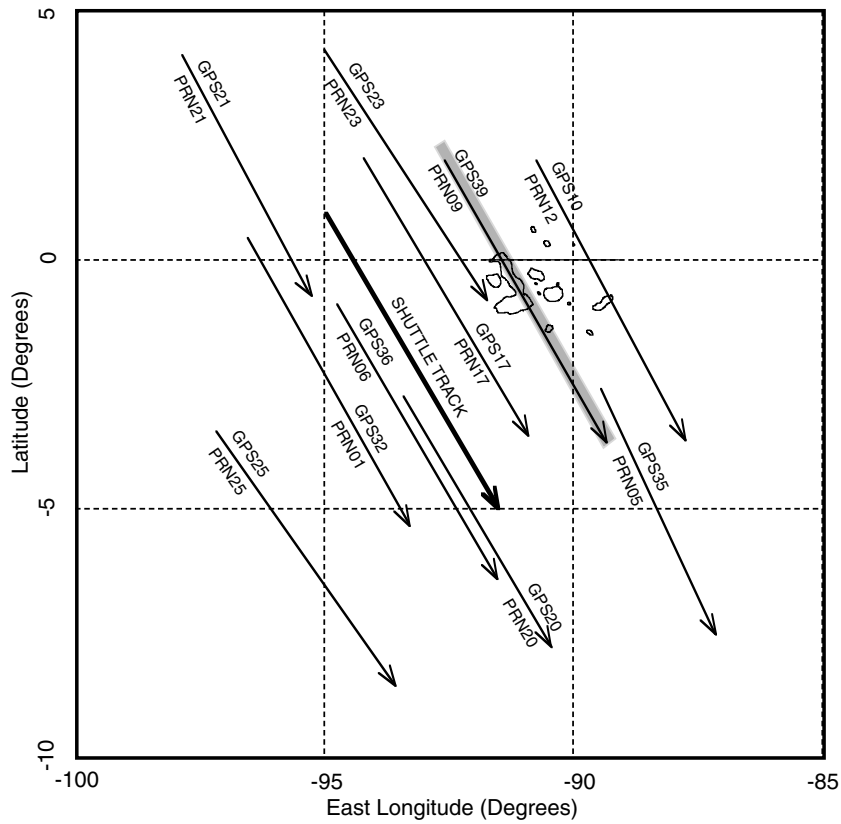


Figure 2. The shuttle track (thick line) over the Pacific Ocean near the Galapagos Islands (shown). Other lines indicate the movement of the specular reflection points on the surface over the several-minute data collection pass. The gray area represents the SIR-C imaging swath and shows how it closely tracks the specular reflection point of GPS39. All tracks shown move southeast with increasing time.

the specular point. Such an ellipse is referred to as an isorange ellipse, and the sizes of the semimajor and semiminor axes corresponding to a 1-Y-chip delay (97.75 ns), 8.1 km and 4.5 km, respectively, are also shown. Figure 3b illustrates the isorange ellipses in greater detail, along with iso-Doppler hyperbolas, which are those points on the surface whose reflected signal arrives at the receiver with the same Doppler frequency shift as compared to the specular reflection. The right-handed, orthonormal coordinate system used in this analysis is also shown centered on the specular reflection point, where the z axis is normal to the surface and the x axis points toward the receiver and is in the same plane as the receiver and transmitting satellite (and this uniquely defines the y axis).

2.3. SIR-C Raw Data

[10] The raw, high-resolution-mode SIR-C data were collected by down-converting the radio frequency (RF)

signal from the antenna using a 1259.91936 MHz local oscillator (LO). The resulting baseband signal was filtered to accept lower sideband frequencies from approximately -40 MHz to DC and sampled with 8-bit resolution at 89.99424 MHz. The LO frequency is hardware-fixed to be 14 times the sampling frequency. These data were not continuously sampled: A 1395-Hz clock drove the collection and recording of 15,624-sample data “lines,” which was equivalent to alternately recording 15,624 samples and ignoring the following 48,888 samples. This was done to window the data collection around the expected SIR-C radar returns but, for our purposes, resulted in data loss and a more difficult analysis.

[11] The Galapagos Island track began with 3 s of calibrations, of which 1 s is receive-only data relevant for our search. This is followed by 110 s of radar-on mapping data, followed by 4 s of receive-only data. The 1- and 4-s receive-only data segments and the first 20 s of the radar-on segment were obtained from the SIR-C

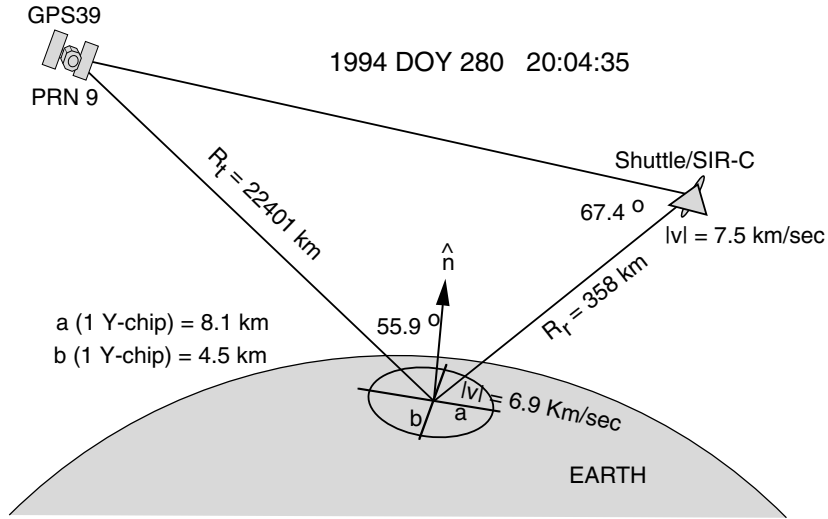


Figure 3a. Specific geometry for the SIR-C Galapagos Islands 4-s calibration data used for this analysis (not to scale). Relevant distances and angles are shown along with the 1-Y-chip isorange contour, as described in the text.

archives. Our signal search used only the 4-s segment because the geometry appeared better than the 1-s segment and more data were available to extract a weak signal.

3. GPS Signal Detection

3.1. Signal Search

[12] In general, a signal search such as this involves cross-correlating the complex conjugate of a phasor model of the desired signal $\mathbf{M}(t)$ with the data $D(t)$ and integrating, resulting in a phasor \mathbf{S} . When the model, which is usually a function of parameters, most closely approximates the data, the amplitude of \mathbf{S} will obtain its

maximum value. A search for significantly large amplitudes of \mathbf{S} as a function of the model parameters is used to detect the signal and determine the optimal set of model parameters for the data. Typically, data sets are divided into smaller segments, and \mathbf{S} is calculated for each segment. The amplitudes of each \mathbf{S} are then summed over the segments to form the final amplitude. Dividing the data up in this manner is done to minimize the effect of mismodeling in \mathbf{M} , which commonly occurs because of the signal having incoherent phase behavior, and to significantly reduce the number of trial model parameter values necessary for signal detection.

[13] A number of search strategies for the SIR-C signal were attempted without success. The first searches

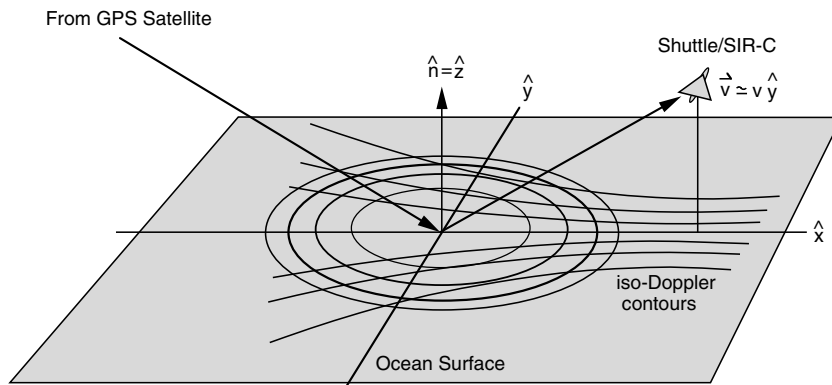


Figure 3b. Iso-Doppler and isorange curves (not to scale) and the coordinate system used in this paper.

focused on maximizing the detection voltage signal-to-noise ratio (SNR) and covered the expected range of geometric modeling error values. The relevant geometric model uncertainties were the shuttle's position and velocity, the position and velocity of the transmitting GPS satellite, errors in the World Geodetic System (WGS 84) [Defense Mapping Agency, 1984] model of the Earth's surface, and atmospheric propagation delays. The 3σ uncertainty in the shuttle's position and velocity during the Galapagos Island track was 1.0 km and 1.0 m s^{-1} , respectively [Rockwell STSOC, 1992, 1997] and thus dominated all other geometric and atmospheric error sources. Several different searches covering this range (and much larger ranges) of geometric modeling errors produced no signal. At the time, we did not know whether our SNR was too low for signal detection, the model errors were larger than we expected, or our untested program (because there was no signal for testing) contained a significant error.

[14] The last search, as this finally detected the signal, focused on hardware parameters, specifically the clock and LO frequency. To search over large clock offsets in a manageable amount of computer time (weeks) required using a very small portion of the data and hoping the SNR was high enough for signal detection. Specifically, the search strategy was to cross-correlate and coherently integrate a single 0.01-s data segment with the model phasor's complex conjugate.

3.2. Derivation of the Model Correlation Phasor

[15] An idealized version of the direct received signal is taken as the model correlation phasor. The equation for the idealized signal is derived by tracing the transmitted signal through its propagation delay, down-conversion to baseband, and sampling, with parameters for hardware clock errors, LO frequency errors, and geometric delay model errors. All transmission gain and loss factors are dropped as they only contribute an overall scaling factor, and all media effects are explicitly ignored, as their effects are absorbed by the delay and phase error parameters. The model is derived for a direct, GPS satellite-to-receiver signal; however, the model search parameters are general enough to efficiently detect reflected signals as well. The signal transmitted by a GPS satellite, $T(t)$, can be written [Spilker, 1980]

$$T(t) = e^{i(\omega_{L2}t + \phi_{L2})} Y(t) D(t), \quad (1)$$

where ω_{L2} is the L2 carrier frequency in radians per second, ϕ_{L2} is a transmitter phase offset in radians, $Y(t)$ is

the transmitted Y code, $D(t)$ is the GPS navigation data message, and t is GPS time. Both $Y(t)$ and $D(t)$ take values ± 1 , depending on t , with Y and D having chip/bit rates of 10.23 MHz and 50 Hz, respectively. The received signal $R(t)$ is

$$R(t) = T[t - \tau^R(t)], \quad (2)$$

where $\tau^R(t)$ is the retarded geometric delay. The instantaneous delay $\tau(t)$ is calculated directly from the model transmitter and receiver positions (and the model ocean height, for the reflected signal). The instantaneous delay is defined by the iterative equation:

$$\tau(t) = \frac{1}{c} |\mathbf{X}_R[t + \tau(t)] - \mathbf{X}_T(t)|, \quad (3)$$

where \mathbf{X}_R and \mathbf{X}_T are the receiver and transmitter position vectors and c is the speed of light. The instantaneous and retarded delays can be written in terms of each other using

$$\begin{aligned} \tau^R(t) &= \tau[t - \tau^R(t)], \\ \tau(t) &= \tau^R[t + \tau(t)]. \end{aligned} \quad (4)$$

[16] After receiving the signal, it is down-converted to baseband by mixing with the receiver's local oscillator. The baseband signal $B(t)$ can be written

$$\begin{aligned} B(t) &= R(t) e^{-i(\omega_{LO}t + \phi_{LO})} \\ &= T[t - \tau^R(t)] e^{-i(\omega_{LO}t + \phi_{LO})} \\ &= \exp(i\{\omega_{L2}[t - \tau^R(t)] + \phi_{L2}\}) \\ &\quad \cdot e^{-i(\omega_{LO}t + \phi_{LO})} Y[t - \tau^R(t)] D[t - \tau^R(t)] \\ &= e^{i(\phi_{L2} - \phi_{LO})} e^{i(\omega_{L2} - \omega_{LO})t} e^{-i\omega_{L2}\tau^R(t)} \\ &\quad \cdot Y(t - \tau^R(t)) D[t - \tau^R(t)], \end{aligned} \quad (5)$$

where ω_{LO} is the receiver LO frequency in radians per second and ϕ_{LO} is an LO phase offset in radians. Physically, the terms in the last line of (5) show, from left to right, a phase offset term, the L2 carrier down-converted by the receiver's LO, a Doppler phase effect due to transmitter and receiver motions, and the retarded chip/bit codes. It should be emphasized that for this derivation, ω_{LO} is the true receiver LO frequency and $\tau^R(t)$ is the true retarded geometric delay.

[17] After mixing with the LO, the receiver samples the baseband signal and records the discrete results. If N samples are recorded, the k th idealized data phasor \mathbf{d}_k can be written

$$\mathbf{d}_k = B(t_0 + k\Delta t) \quad k = 0, N-1, \quad (6)$$

where t_0 is the time of the first ($k = 0$) sample and Δt is the true sampling interval. With these definitions, \mathbf{d}_k can be written

$$\mathbf{d}_k = \exp\{i[\phi_{L2} - \phi_{LO} + (\omega_{L2} - \omega_{LO})t_0]\} \cdot \exp\{i[(\omega_{L2} - \omega_{LO})k\Delta t - \omega_{L2} \tau^R(t_0 + k\Delta t)]\} \cdot Y[t_0 + k\Delta t - \tau^R(t_0 + k\Delta t)]D['], \quad (7)$$

where $D[']$ implies that D 's argument is identical to Y 's. The following definitions relate the nominal and true values:

$$\begin{aligned} t_0 &\equiv p_0 + \tau_c, \\ \Delta t &\equiv \Delta p(1 + \dot{\tau}_c), \\ \omega_{LO} &\equiv \omega_{LO}^n(1 + \dot{\tau}_c)^{-1} + \Delta\omega, \end{aligned} \quad (8)$$

where p_0 is the nominal time of the first sample, fixed by the time tag information accompanying the data, Δp is the nominal sampling interval, fixed to $(89.99424 \text{ MHz})^{-1}$, and ω_{LO}^n is the nominal LO frequency, fixed to $14 \times 89.99424 \text{ MHz} = 1259.91936 \text{ MHz}$. The τ_c , $\dot{\tau}_c$, and $\Delta\omega$ parameters represent the clock error, clock rate error, and residual frequency error, respectively. The $(1 + \dot{\tau}_c)^{-1}$ term in the last line of (8) accounts for the fact that the sampling and LO frequencies have a fixed, hardware-established ratio of 14; that is, the signal is sampled every 14 LO cycles. The $\Delta\omega$ parameter could absorb this effect, but the formulation given by (8) makes $\Delta\omega$ independent of $\dot{\tau}_c$. Finally, $\tau^R(t)$, the true retarded delay, can be written

$$\tau^R(t) \equiv \tau^{Rm}[t - \Delta\tau - \Delta\dot{\tau}(t - t_0)] + \Delta\tau + \Delta\dot{\tau}(t - t_0), \quad (9)$$

where τ^{Rm} is the retarded delay model, $\Delta\tau$ is a constant model delay error, and $\Delta\dot{\tau}$ is a constant model delay rate error. This assumes that any relevant model errors in τ^{Rm} can be accurately described by the linear expression $\Delta\tau + \Delta\dot{\tau}(t - t_0)$ and higher-order effects are negligible. The reason for the $\Delta\tau$ and $\Delta\dot{\tau}(t - t_0)$ terms in the argument of τ^{Rm} will be explained below. The k th idealized data phasor can now be written

$$\begin{aligned} \mathbf{d}_k &= \exp\left(i\left\{\phi_{L2} - \phi_{LO} + \left[\omega_{L2} - \omega_{LO}^n(1 + \dot{\tau}_c)^{-1} - \Delta\omega\right] \cdot (p_0 + \tau_c) - \omega_{L2}\Delta\tau \right. \right. \\ &\quad + \left[\omega_{L2} - \omega_{LO}^n(1 + \dot{\tau}_c)^{-1} - \Delta\omega - \omega_{L2} \Delta\dot{\tau}\right] \cdot \Delta p(1 + \dot{\tau}_c)k - \omega_{L2} \tau^{Rm} \\ &\quad \cdot [p_0 + \tau_c - \Delta\tau + (1 - \Delta\dot{\tau})\Delta p(1 + \dot{\tau}_c)k]\} \Big\} \\ &\quad \cdot Y\{p_0 + \tau_c - \Delta\tau + (1 - \Delta\dot{\tau})\Delta p(1 + \dot{\tau}_c) \cdot k - \\ &\quad \tau^{Rm}[p_0 + \tau_c - \Delta\tau + (1 - \Delta\dot{\tau})\Delta p(1 + \dot{\tau}_c)k]\}D[']. \end{aligned} \quad (10)$$

The parameters τ_c , $\dot{\tau}_c$, $\Delta\omega$, $\Delta\tau$, and $\Delta\dot{\tau}$ are assumed to be time independent: Any higher-order, nonlinear behavior over the 4-s SIR-C data interval is assumed negligible.

[18] The five parameters in (10) are degenerate in that changes in some of them can be absorbed by the others, to the degree of accuracy available in the 4-s SIR-C data interval. Two of these parameters are eliminated: The geometric delay model error, $\Delta\tau \leq 2 \mu\text{s}$, and the geometric delay rate model error, $\Delta\dot{\tau} \leq 2 \text{ ns/s}$, will be absorbed by the other three parameters, τ_c , $\dot{\tau}_c$, and $\Delta\omega$. The “clock” parameters, $\bar{\tau}_c$ and $\bar{\dot{\tau}}_c$, will then describe both physical clock effects and geometric model delay errors, and the residual frequency error $\bar{\Delta\omega}$ will absorb any Doppler-induced behavior of the geometric model error. The new parameters are defined by

$$\begin{aligned} \bar{\tau}_c &\equiv \tau_c - \Delta\tau, \\ \bar{\dot{\tau}}_c &\equiv \dot{\tau}_c - \Delta\dot{\tau}, \\ \bar{\Delta\omega} &\equiv \Delta\omega(1 + \Delta\dot{\tau}). \end{aligned} \quad (11)$$

Substituting these into (10) gives the idealized k th data sample:

$$\begin{aligned} \mathbf{d}_k &= \exp\left\{i\left[\phi_0 + \left(\omega_{L2} - \omega_{LO}^n(1 + \bar{\dot{\tau}}_c)^{-1} - \bar{\Delta\omega}\right) \cdot \Delta p(1 + \bar{\dot{\tau}}_c)k - \omega_{L2}\tau^{Rm} \right. \right. \\ &\quad \cdot [p_0 + \bar{\tau}_c + \Delta p(1 + \bar{\dot{\tau}}_c)k]\} \Big\} \\ &\quad \cdot Y[p_0 + \bar{\tau}_c + \Delta p(1 + \bar{\dot{\tau}}_c)k \\ &\quad - \tau^{Rm}(p_0 + \bar{\tau}_c + \Delta p(1 + \bar{\dot{\tau}}_c)k)]D['], \end{aligned} \quad (12)$$

where all time-independent phase terms are grouped into ϕ_0 and second-order terms are neglected. This explicitly shows that linear clock errors can absorb geometric delay errors if, as noted above, the geometric errors retard the model time tag, as shown in (9). Note that shifting k by l samples (lags) is equivalent to changing $\bar{\tau}_c$ by $\Delta p(1 + \bar{\dot{\tau}}_c)l$. This fact is exploited to rapidly search over the $\bar{\tau}_c$ parameter range using fast Fourier transform (FFT) techniques, described below in section 3.4. Finally, the retarded delay is expanded about the first-sample time. Rearranging terms leads to

$$\begin{aligned} \mathbf{d}_k &= \exp\left(i\left\{\phi_0 - \omega_{L2}\tau^{Rm}(p_0 + \bar{\tau}_c) \right. \right. \\ &\quad + \left[\omega_{L2} - \omega_{LO}^n(1 + \bar{\dot{\tau}}_c)^{-1} - \bar{\Delta\omega} - \omega_{L2}\dot{\tau}^{Rm}(p_0 + \bar{\tau}_c)\right] \cdot \Delta p(1 + \bar{\dot{\tau}}_c)k \Big\} \Big\} \\ &\quad \cdot Y\left\{p_0 + \bar{\tau}_c - \tau^{Rm}(p_0 + \bar{\tau}_c) \right. \\ &\quad \left. + [1 - \dot{\tau}^{Rm}(p_0 + \bar{\tau}_c)]\Delta p(1 + \bar{\dot{\tau}}_c)k\right\}D[']. \end{aligned} \quad (13)$$

The model phasor used in this analysis, \mathbf{M}_k is a slightly modified form of (13). The constant phase $\phi_0 - \omega_{L2}\tau_c^{Rm}$ ($p_0 + \bar{\tau}_c$) in (13) is dropped because the overall phase has no effect on the analysis presented in this paper. The data bit function $D(t)$ in (13) is also dropped, as this function's effect is negated in the signal search and is explicitly handled in the remainder of the analysis. The k th model phasor, \mathbf{M}_k , is given by

$$\begin{aligned} \mathbf{M}_k = \exp \Big\{ & i \left[\omega_{L2} - \omega_{LO}^n (1 + \bar{\tau}_c)^{-1} - \bar{\Delta\omega} \right. \\ & \left. - \omega_{L2} \dot{\tau}^{Rm} (p_0 + \bar{\tau}_c) \right] \Delta p (1 + \bar{\tau}_c) k \Big\} \\ & \cdot Y \Big\{ p_0 + \bar{\tau}_c - \tau^{Rm} (p_0 + \bar{\tau}_c) \\ & + [1 - \dot{\tau}^{Rm} (p_0 + \bar{\tau}_c)] \Delta p (1 + \bar{\tau}_c) k \Big\}. \end{aligned} \quad (14)$$

3.3. Implementing the Signal Search

[19] The choice of using a 0.01-s data segment was made for several reasons. First, this helped avoid the unmodeled phase transitions encoding the 50-Hz navigation data message. Choosing a 0.01-s data interval results in only a 25% chance of having an unmodeled transition in the data segment, and even if present, there would be little SNR degradation if it occurred near either end of the data interval. To insure against the small possibility that an unmodeled transition in this data interval reduces the SNR below detectable levels, a parallel search, using the next 0.01-s data segment, was started at a lower priority; at least one of the two data segments was guaranteed to have no such transition. A 0.01-s data segment also allowed a simultaneous search for the direct and reflected signals. Because no detailed information on the SIR-C antenna beam pattern, other than the overall gain, was in hand at the time of the signal search, it was not known whether the direct, GPS-to-SIR-C signal entering the antenna aperture at a high elevation angle would be stronger than the much weaker reflected signal entering the antenna near its main beam. Choosing a 0.01-s data segment represented a compromise between wanting more data to increase the coherent direct signal SNR and not wanting to integrate the reflected signal too much beyond its expected coherence time of about 1.6 ms (see section 4.2 below for a derivation of our a priori signal coherence time estimate). Finally, 0.01 s of data allowed a search covering ± 1 s in $\bar{\tau}_c$ in about a month using three dedicated DEC 500-MHz Alpha computers.

[20] A specialized software receiver/correlator was created to search specifically for a GPS signal in the

Galapagos data using the model given by (14). Using the nomenclature presented at the beginning of section 3.1, if D_k is the k th data sample and \mathbf{S}_l is the l th signal phasor,

$$\mathbf{S}_l = \sum_{k=0}^{N-1} D_k \mathbf{M}_{k-l}^*, \quad (15)$$

where N is the total number of samples in the integration and l is referred to as the lag number. Because the 0.01-s data segment was composed of 14 data lines, $N = 13 \times (15,624 + 48,888) + 15,624$, and D_k is zero for the 48,888-sample gaps between lines, as described above. Note that \mathbf{S}_l has maximum amplitude when the Y codes of the model and data are temporally aligned, and the model phase counterrotates the data's phase to an approximately constant value, over the N -sample integration. The parameter of interest is the amplitude of \mathbf{S}_l and can be written as

$$S_l(\bar{\tau}_c, \bar{\tau}_c, \bar{\Delta\omega}) = \left| \sum_{k=0}^{N-1} D_k \mathbf{M}_{k-l}^*(\bar{\tau}_c, \bar{\tau}_c, \bar{\Delta\omega}) \right|, \quad (16)$$

where $\bar{\tau}_c$, $\bar{\tau}_c$ and $\bar{\Delta\omega}$ are the three search parameters.

3.4. Using Fourier Transforms to Speed Lag Calculations

[21] Equation (15) can be calculated quickly, for a large number of lags, using FFT techniques, as shown in Appendix A. The signal search used FFTs to efficiently calculate \mathbf{S}_l for $2^{23} - 13$ $(15,624 + 48,888) - 15,624 = 7,534,328$ lags with fixed search parameters. The FFT routines operated on arrays of length 2^{23} , where the first 854,280 elements of the data array contained the 14 lines of data (fourteen 15,624-sample lines with 48,888 zero-amplitude phasors in between), followed by 7,534,328 zero-amplitude phasors. The model array contained the model values corresponding to lags from $-3,767,164$ to $4,621,443$ arranged so lags 0 to $4,621,443$ are in their corresponding array elements, while model values for lags $-3,767,164$ to -1 are in array elements $4,621,444$ to $8,388,607$, assuming the array elements are numbered from 0 to $2^{23} - 1$. Arranging the array elements in this way results in the proper correlation calculation for lags $-3,767,164$ to $3,767,164$, inclusive. Because of the cyclic nature of the FFT the remaining 854,279 lags are improper in that they correspond to data being correlated across the model's temporal discontinuity at lag $4,621,444$ and are discarded.

[22] The choice of using 2^{23} array element FFTs was not arbitrary; a power of two is required for the FFT algorithm, and 2^{23} was chosen to maximize the search efficiency. The FFT execution time scales as $N \log N$, for large N , so fast Fourier transforming 2^k -element arrays twice is faster than transforming a 2^{k+1} -element array once. On the other hand, inefficiencies and overhead in the FFT algorithm and, in this case, the inefficiency of discarding the improper correlations require larger arrays for higher overall efficiency. For this analysis it was empirically determined that 2^{23} -element arrays were most efficient.

[23] As noted above, searching over $\bar{\tau}_c$ is equivalent to searching over lag; the relationship between them being $\bar{\tau}_c = \Delta p(1 + \bar{\tau}_c)l$. The FFT lag calculation was repeated for clock rates $\bar{\tau}_c$ between $\pm 0.1 \mu\text{s s}^{-1}$ in steps of $\pm 0.01 \mu\text{s s}^{-1}$ and $\Delta\omega$ values between ± 30 Hz in 10-Hz steps, where the maximum value of S_l for each lag, S_l^{\max} , was noted, along with the corresponding $\bar{\tau}_c$ and $\Delta\omega$ values. The above calculations were repeated for $\bar{\tau}_c$ values incremented in steps of 7,480,000 lags: The small overlap in calculated lag values was used to ensure no gaps in the $\bar{\tau}_c$ search due to the $(1 + \bar{\tau}_c)$ term in the relationship between lag and $\bar{\tau}_c$. Finally, the S_l^{\max} values were normalized by removing their mean, $\langle S_l^{\max} \rangle$, and dividing by their standard deviation, $\sigma_{S_l^{\max}}$:

$$\bar{S}_l^{\max} \equiv \frac{(S_l^{\max} - \langle S_l^{\max} \rangle)}{\sigma_{S_l^{\max}}}, \quad (17)$$

where \bar{S}_l^{\max} are the normalized amplitudes. In this way, the signal search was reduced to searching for significant values of \bar{S}_l^{\max} .

3.5. Search Results

[24] After performing approximately 2.9×10^{10} lag correlations, the search described in sections 3.1–3.4 found a signal with a large model clock error parameter: $\bar{\tau}_c = 1.164$ s. Once the signal was found, the entire 4-s data set was used to optimize the search parameters. The signal was found to persist throughout the 4-s data set and maintain a constant peak lag. The optimal clock rate error and residual frequency error were found well outside the search range: $\bar{\tau}_c = 1.729 \mu\text{s s}^{-1}$ and $\Delta\omega = 497$ Hz. The large clock parameter values were later explained by the instrument clock having a frequency standard much worse than was assumed. The discrepancy between the clock value found and the SIR-C value is consistent with the instrument clock being set to the shuttle clock on power-up and the instrument clock drifting for several days to accumulate a >1-s difference.

If the clock rate is assumed constant, dividing the measured clock rate into the measured clock offset predicts 7.8 days of clock drift, close to the mission elapsed time of 7.4 days for our data epoch. The residual frequency error was also unexpectedly high and initially could not be explained by either geometric model errors or LO frequency drift. Further analysis, presented below in section 4.3, which includes a detailed model of the antenna beam pattern obtained from the SIR-C mission, almost exactly explains this anomalous value as a beam-steering effect which could only be obtained from the reflected signal.

[25] Figure 4a shows the normalized amplitude as a function of lag for the model parameters given above, but with 0.174-ms coherent integrations, corresponding to a single 15,624-sample data line, with the 5580 resulting amplitudes summed over the full 4 s of data. The plot is normalized so that lags far from the signal have zero mean and unit variance, so this is also a plot of voltage SNR, where a peak SNR of 334 is observed.

[26] After finding the 4-s signal, a signal search was performed on the 1-s data segment at the beginning of the Galapagos Island track. This search was successful and led to the signal shown in Figure 4b, having about 5 times the width of that found in the 4-s data set and a peak SNR of about 10 (combining several adjacent points would increase the SNR of this signal). The clock, clock rate, and frequency offset parameters which maximize the 1-s peak are 1.1638132 s, $1.729 \mu\text{s s}^{-1}$, and -2740 Hz, respectively. Because the peak amplitude here is only weakly dependent on the clock rate parameter, and because the range of clock rate parameters that give essentially identical maximum peak values includes the value found for the 4-s signal analysis, this parameter was fixed to the 4-s signal value. It will be shown in section 4.3 below that, compared to the 4-s waveform, the degradation of the signal amplitude and the factor of 5 wider signal shape are due to a geometric effect: The antenna points much further away from the specular point at this epoch than in the 4-s case.

[27] The radar-on data were also searched using an incoherent sum over the entire 20 s, but no signal was found. No further investigation or analysis has been done with the radar-on data.

4. Evidence for a Reflected Signal

[28] Because of the unique nature of the Y code the signals shown in Figures 4a and 4b must be from GPS 39, having PRN 9; however, there is the logical possibility that these are direct, GPS-to-SIR-C signals. This

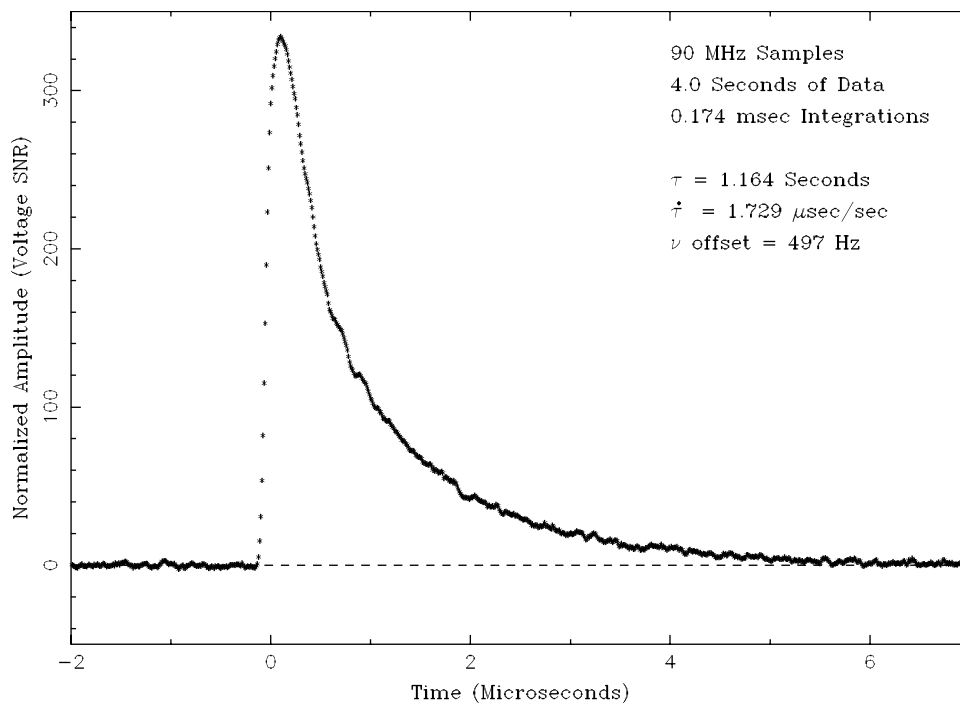


Figure 4b. Final reflected signal from GPS39, having PRN 9, from the 1-s data segment. The data points (stars) are spaced by 11.11 ns, and each star is a lag, as indicated in (17). The model parameters maximizing the normalized amplitude (voltage SNR) are also indicated. The lag corresponding to zero time is arbitrary.

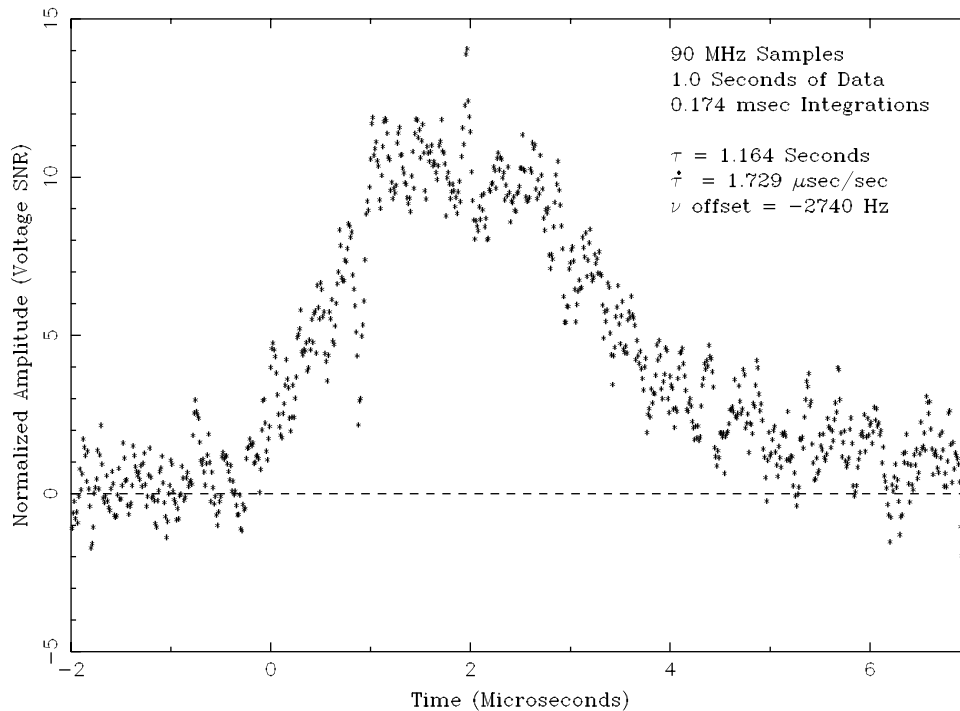


Figure 4b. Final reflected signal from GPS39, having PRN 9, from the 1-s data segment. The data points (stars) are spaced by 11.11 ns, and each star is a lag, as indicated in (17). The model parameters maximizing the normalized amplitude (voltage SNR) are also indicated. The lag corresponding to zero time is arbitrary.

could be clarified immediately if two signals were observed in both data sets with the expected time delay between them, but an extensive search in the 4-s data has failed to yield the direct signal (or the “reflected” signal, if this were the direct signal). There are three pieces of evidence supporting the reflected-signal hypothesis and contradicting the direct signal hypothesis: (1) The signals’ temporal shapes agree with that expected from a detailed simulation of the reflection geometry, scattering process, and antenna beam pattern but do not agree with the approximately triangular shape expected for a direct signal. This is true for both the 1-s and 4-s data segments, which have observation geometries different enough to produce the very different waveforms shown in Figures 4a and 4b. (2) The 4-s signal’s measured coherence time is about 1.0 ms, in agreement with that expected for the reflected signal, and completely inconsistent with the direct signal hypothesis. (3) The 497- and -2740-Hz residual frequency errors, too large to be explained by geometric-modeling or hardware LO frequency errors, are explained by the footprint of the antenna beam pattern on the ocean surface pointing away from the specular point along higher-frequency iso-Doppler contours.

[29] These points will be examined in more detail, where the evidence clearly indicates we have observed reflected GPS signals. We also specifically address, and eliminate, three mechanisms by which a corrupted direct signal could potentially produce the waveform shown in Figure 4a. In particular, we show that the observed signal is not a direct signal corrupted by second-order modeling errors, shuttle multipath scattering, or the recording band-pass not containing all of the Y code spread spectrum.

4.1. Signal’s Temporal Shape

[30] The measured signals’ temporal shape is quite different from that expected for a direct signal. A direct signal would approximate the Y code autocorrelation function, a triangle with a rise and fall time of about $0.09775 \mu\text{s}$, but with its slope discontinuities smoothed by the limited GPS transmission band pass and the SIR-C receiver band pass. A model was created for the expected direct signal which includes the limited GPS transmitter band pass, the SIR-C band pass which cuts off a small portion of the Y code spread spectrum, and the Y code autocorrelation properties. Figures 5a and 5b compare the measured signals with the expected direct signal, showing that the measured peaks are about 7 and 30 times wider than expected and do not agree with the direct signal hypothesis.

[31] To predict the temporal shape of a reflected signal requires a model of the reflection process. This model begins with a special form of the bistatic radar equation [e.g., *Zavorotny and Voronovich*, 2000] and uses the geometric optics limit of the Kirchhoff approximation. The model power for a single, 0.174-ms coherent integration $C(\tau)$ is given by

$$C(\tau) = c_0 \int \frac{G(\rho)\Lambda^2(\tau - \tau^R)\text{sinc}^2[T_I\Delta f_D(\rho)]}{4\pi R_t^2 R_r^2} \sigma_0^p(\rho) d\rho, \quad (18)$$

where c_0 is a constant scale factor described below, τ is the lag delay, ρ is a vector spanning the ocean’s surface relative to the specular point $G(\rho)$ is the antenna gain pattern projected onto the surface, $\Lambda(t)$ is the triangular Y code autocorrelation function, $\text{sinc}(x) \equiv \sin(\pi x)/(\pi x)$, T_I is the coherent integration time of 0.174 ms, Δf_D is the Doppler frequency shift relative to the specular point, $\sigma_0^p(\rho)$ is the scattering cross section for polarization p , R_t is the distance from the GPS transmitter to the specular point, and R_r is the distance from the receiver to the specular point. Although the ocean must be considered a multiscale rough surface, as small waves ride upon larger ones, the large roughness scales (big waves) predominate at scattering directions close to the specular point, particularly in the high-frequency limit. In this case, surface curvature effects can be neglected, and the scattered field can be evaluated by solving the Stratton-Chu integral equation using the Kirchhoff approximation [Ulaby *et al.*, 1982; Bass and Fuks, 1979]. The bistatic cross section coefficient for this measurement is then taken to be

$$\sigma_0^{rs}(\rho) = \frac{(kq|U_{rs}|)^2}{q_z^4 \langle S^2 \rangle} e^{-(q_z^2 + q_y^2)/\langle S^2 \rangle}, \quad (19)$$

where r, s indicate the polarization state, either vertical or horizontal, k is the GPS carrier wave number, $\langle S^2 \rangle$ is the mean-square slope of the sea surface, discussed below, \mathbf{q} is given by

$$\mathbf{q} = k(\mathbf{n}_s - \mathbf{n}_i), \quad (20)$$

where \mathbf{n}_s and \mathbf{n}_i are the unit vectors in the direction of the scattered and incident field, respectively, and $q \equiv |\mathbf{q}|$. The functions U_{rs} are the scattering matrix components, reported by Ulaby *et al.* [1982], [volume 2, chapter 12], and depend on the incident and scattering directions defined there. These functions contain the Fresnel reflection coefficients for the air-sea planar interface, defined, for example, by Stratton [1941]. Our model for the sea is also parameterized for salinity and temperature

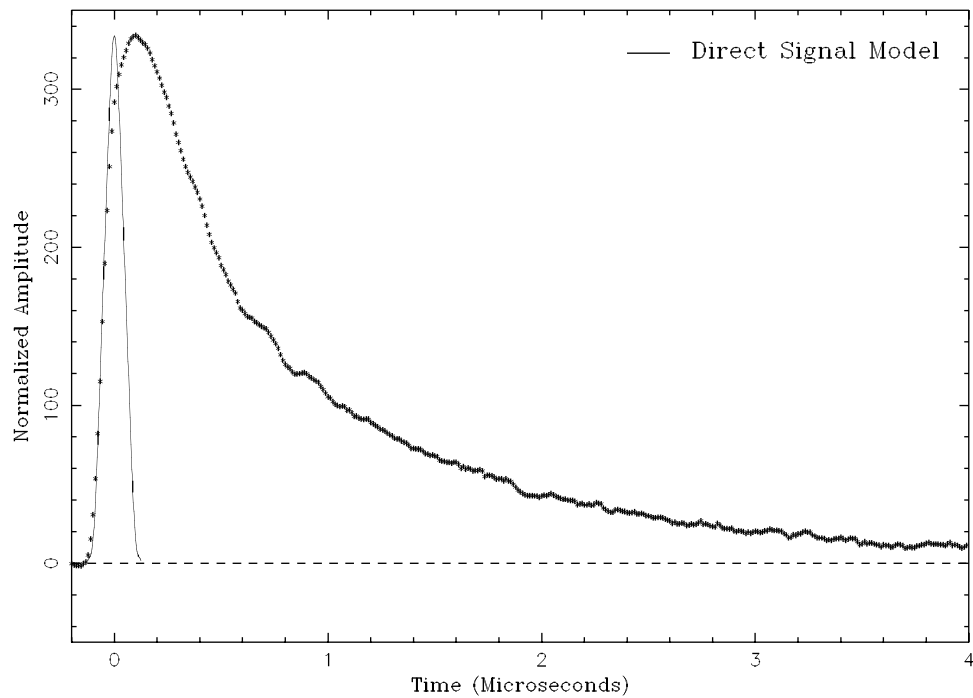


Figure 5a. The 4-s signal (stars) with the expected signal for the direct, GPS39-to-SIR-C path (solid curve), scaled to have the same peak amplitude. The measured signal is clearly not consistent with that expected from the direct signal.

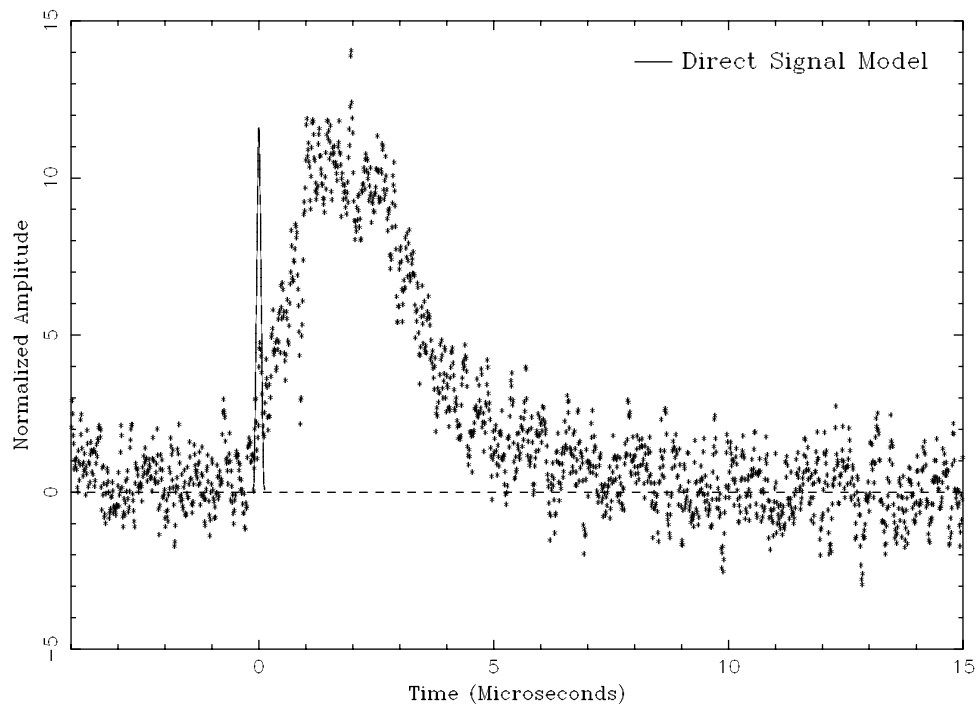


Figure 5b. The 1-s signal (stars) with the expected signal for the direct, GPS39-to-SIR-C path (solid curve), scaled to have the same peak amplitude. The measured signal is clearly not consistent with that expected from the direct signal.

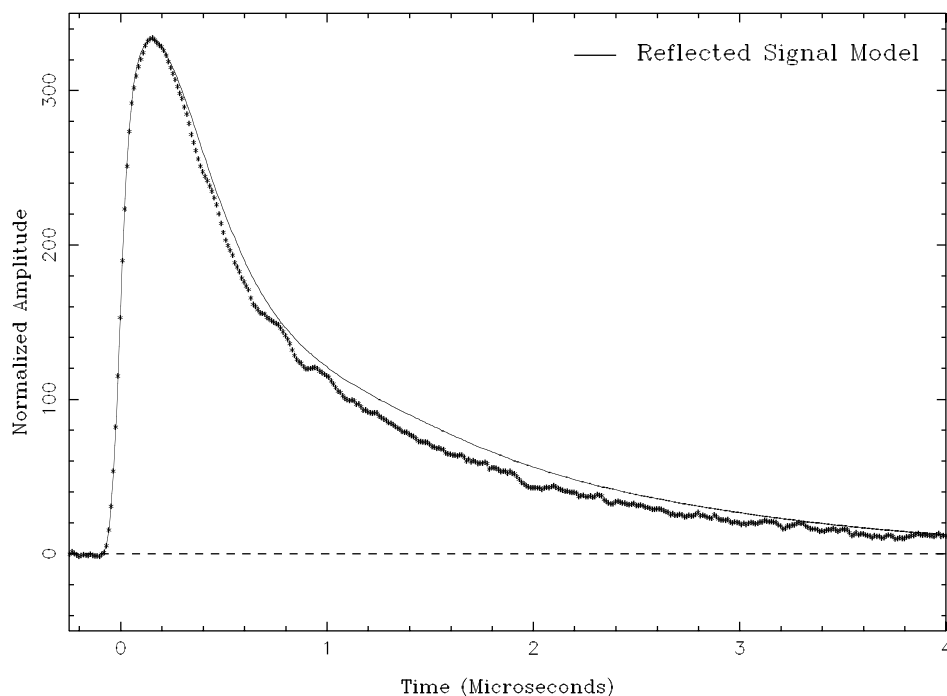


Figure 5c. The 4-s signal (stars) with the reflected-model waveform (solid curve). The agreement between the data and the reflection model is reasonably good; the small discrepancy is probably due to errors in the scattering cross section, the antenna gain pattern model, or Earth curvature effects.

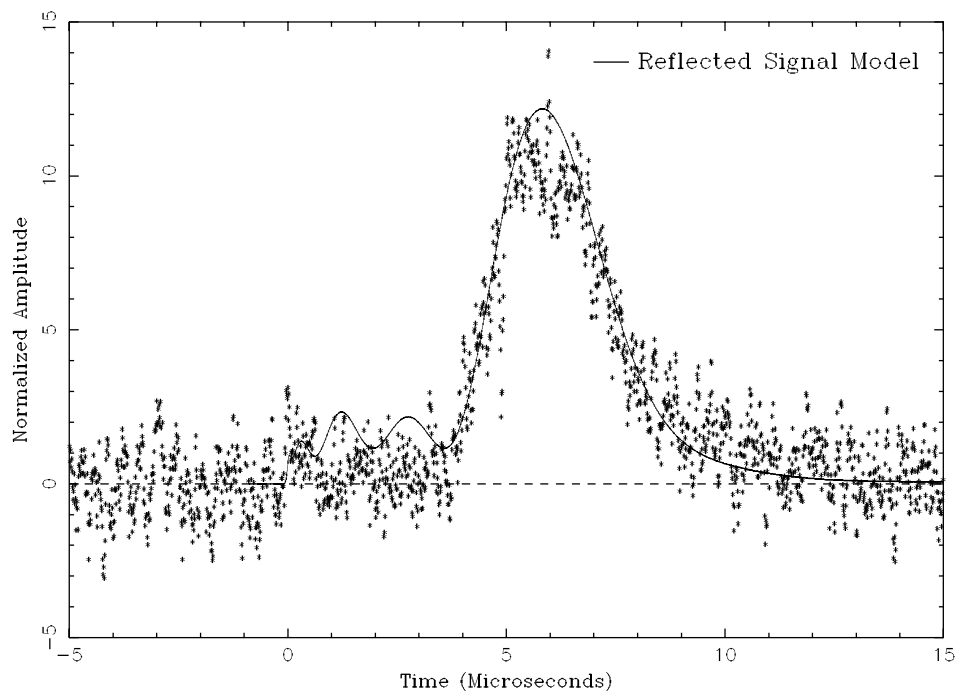


Figure 5d. The 1-s signal (stars) with the reflected-model waveform (solid curve). Zero on the timescale represents the expected specular return. The arbitrary scaling constant, c_0 , was 40% of that found for the 4-s signal. The agreement between the data and the reflection model is reasonably good. The discrepancy between the 1-s to 4-s c_0 values is probably due to Earth-curvature effects or errors in the scattering cross section.

according to *Klein and Swift* [1977]. Since (18) is written for an unspecified linear polarization, a general expression for circular polarization can be obtained starting with the following transformation between right/left circular (rc/lc) polarizations and horizontal/vertical (h/v) polarizations for the electric fields E :

$$\begin{pmatrix} E_{rc} \\ E_{lc} \end{pmatrix} = \frac{1}{\sqrt{2}} \begin{pmatrix} 1 & i \\ 1 & -i \end{pmatrix} \begin{pmatrix} E_h \\ E_v \end{pmatrix}. \quad (21)$$

Applying it to the scattering matrix, we can obtain the scattering matrix for circular polarization between the transmitted and received fields:

$$\begin{pmatrix} E_{rc}^{rec} \\ E_{lc}^{rec} \end{pmatrix} = \frac{1}{2} \begin{pmatrix} U_{hh} + U_{vv} + i(U_{vh} - U_{hv}) & U_{hh} - U_{vv} + i(U_{vh} + U_{hv}) \\ U_{hh} - U_{vv} - i(U_{vh} + U_{hv}) & U_{hh} + U_{vv} - i(U_{vh} - U_{hv}) \end{pmatrix} \cdot \begin{pmatrix} E_{rc}^{tran} \\ E_{lc}^{tran} \end{pmatrix}, \quad (22)$$

which indicates the presence of like-polar and unlike-polar components depending on the incident and scattered directions. For the specific case presented here, the SIR-C antenna collected horizontally polarized signals. Thus an inversion of (21) was performed to convert the right circular GPS transmitted signals into the desired horizontal received component.

[32] In (19) the effect of the sea surface appears via the mean-square slope $\langle S^2 \rangle$, a wind-dependent quantity. Using $\Psi(k_x, k_y)$ to indicate the sea elevation spectrum, defined as the Fourier transform of the autocorrelation function of the surface displacement, and hence a function of the surface spectral components, the omnidirectional mean square slope is defined as

$$\langle S^2 \rangle = \int_{-\infty}^{\infty} \int_{-\infty}^{\infty} \kappa_s^2 \Psi(\kappa_x, \kappa_y) d\kappa_x d\kappa_y, \quad (23)$$

where $\kappa_s^2 \equiv \kappa_x^2 + \kappa_y^2$, and κ_x , and κ_y , refer to the sea spectral wave numbers. It should be stressed that the scattering model outlined above is strictly valid in the high-frequency (geometry optics) limit. For a microwave instrument operating at the electric wave number k , it has been proposed that the relevant mean-square slope is not the total slope, but rather the component resulting from the integration of the low spectral wave numbers up to a cutoff point which depends on the electric wave number k . Historically, the cutoff has been taken at $k/3$ [Brown, 1977] on the grounds that the instrument is not sensitive to higher spectral components. Recently, *Zavorotny and Voronovich* [2000] calculated $\langle S^2 \rangle$

assuming the sea spectrum of *Elfouhaily et al.* [1997], truncated according to *Brown* [1977], to model the GPS scattered signal received from an aircraft in nadir looking geometry as affected by wind speed. One must note that the calculated $\langle S^2 \rangle$ in this case is very sensitive to the chosen truncation point. We have seen that although the effect of wind speed on the spectrum is complicated, it can be reduced to one parameter when one of the spectrum's moments, $\langle S^2 \rangle$, is considered instead. Indeed sea spectra are validated by calculations of their $\langle S^2 \rangle$, and credible spectral distributions are constrained by having to comply with measured mean-square slopes. However, many uncertainties are present in the assumptions for the sea spectra, so much that various accepted spectra produce conflicting $\langle S^2 \rangle$. As an alternative approach, spectrum-independent empirical $\langle S^2 \rangle$ resulting from data fitting have been used for some time; a compendium of results is presented by *Elfouhaily et al.* [1997]. While we have used in our current model the same $\langle S^2 \rangle$ as given by *Zavorotny and Voronovich* [2000], we expect some limitation of accuracy from this representation, stemming from the concerns described above. However, we believe that the general trend of our results holds since the waveform shape is more strongly affected by the antenna pattern than the truncation point, in the geometry examined here.

[33] The function given by (18) is converted to the final, normalized voltage SNR by accounting for the incoherent amplitude summations over the 5580 data lines. This is done using

$$S_v(\tau) = \sqrt{m} \sqrt{\frac{\pi}{4 - \pi}} \left\{ e^{-C(\tau)/4} \left[\left(1 + \frac{C(\tau)}{2} \right) I_0 \left(\frac{C(\tau)}{4} \right) + \frac{C(\tau)}{2} I_1 \left(\frac{C(\tau)}{4} \right) \right] - 1 \right\}, \quad (24)$$

which is derived by *Lowe* [1999], where $m = 5580$ is the number of incoherent amplitude summations and I_0 and I_1 are modified Bessel functions of the first kind. The scale factor c_0 in (18) is adjusted so that the peak SNR of the model and 4-s data agree. It is important that c_0 scales the coherent power in (18), and not the final voltage SNR, because (24) is nonlinear.

[34] Figures 5c and 5d compare the normalized amplitude (voltage SNR) for the 4- and 1-s data and reflection model, given by (24) and (18), using the expected antenna pointing direction. The data clearly agree much more favorably with the reflection model than with the direct signal model.

[35] In the 4-s data, shown in Figure 5c, the model of the signal's tail predicts more power than is observed, especially from 1 to 3 μ s. This is presumably due to uncertainties in our scattering cross section or antenna beam pattern model, or Earth curvature effects which are not completely included in our model (the scattering calculations are done on a plane tangent to the specular point). The waveform's initial rise, which is less sensitive to details of the scattering process, agrees very well with the reflection model. These data also show irregularities not seen in the model, so they are probably not due to the expanding isorange ellipse intersecting antenna sidelobes (which are in the model). Because these data are over-sampled and the Y code autocorrelation function has a finite width, adjacent data points are highly correlated. This results in noise fluctuations having the same width as the direct signal model, shown in Figure 5a, for example. The fluctuations in the data are only slightly greater in amplitude than is expected from noise, making it difficult to interpret them as caused by irregularities in the ocean's surface, although they may be caused by such.

[36] In the 1-s data, shown in Figure 5d, the width of the signal agrees well with the model prediction. The time origin in this figure corresponds to the expected specular return from the model, and the data points are positioned arbitrarily in time to best match the model peak. The model wind speed was fixed to that used in the 4-s model. The c_0 parameter from (18), which arbitrarily scales the signal strength, is about 40% of that found in the 4-s analysis. This discrepancy, which is too large to be due to mismodeling of the wind speed, is most likely due to our scattering calculation having a reflection coefficient that is too large for off-specular geometries, or not including Earth curvature effects.

4.2. Signal's Coherence Properties

[37] The coherence properties of a direct GPS signal are very different from those expected from an ocean-reflected signal observed from low-Earth orbit. The direct signal, observed from space without intervening media effects, would be expected to have a very long coherence time, several orders of magnitude longer than the 4 s of data used for this measurement. The reflected signal's coherence properties are dominated by the receiver's motion through the scattered signal's far field, as described by the van Cittert-Zernike theorem. We roughly estimated the coherence time before initiating our signal search, by assuming that the area on the surface, bounded by the isorange ellipse corresponding to a 1-Y-code delay, was uniformly transmitting. A uniformly illuminated

circular aperture has its first null at an angle of $1.22\lambda_{L2}/D$ rad, where λ_{L2} is the L2 wavelength and D is the diameter of the aperture. This, multiplied by R_r , the distance from the specular point to the receiver, is the perpendicular distance to the first null. Dividing by v_p , the perpendicular velocity, gives an estimate for the coherence time:

$$\tau_{\text{coh}} = \frac{1.22\lambda_{L2}R_r}{Dv_p}. \quad (25)$$

The diameter of the isorange ellipse, as seen from the receiver, is given by

$$D = 2b = 2\sqrt{\frac{2\Delta R_t R_r}{R_t + R_r}}, \quad (26)$$

where b is the radius of the ellipse in the direction of the receiver's velocity, as shown in Figure 3a, R_t is the distance from the specular point to the GPS satellite transmitter, and Δ is the chip length expressed in meters. Using the values shown in Figure 3a, our a priori coherence time estimate τ_{coh} was about 1.6 ms. This time is much less than the correlation time of the moving sea surface, so this latter effect is neglected.

[38] Two aspects of the SIR-C data complicate a measurement of the coherence time. First, the data are not continuously sampled: 15,624-sample data lines are recorded at 1395 Hz, resulting in a 24% duty cycle. This 0.717-ms repetition rate is on the order of the a priori expected coherence time of about 1.6 ms, making coherence measurements difficult. The second difficulty is that even in the 4-s data set which we examine exclusively in this section, the signal SNR is too low to reliably recover the 50-Hz navigation data bit transitions, which introduce random, unmodeled, 180° phase changes into the data.

[39] The usual method of obtaining the navigation-message bits consists of coherently integrating over each 0.02-s data bit and tracking phase. This cannot be done here as each data bit is many times longer than the expected coherence time. The most successful attempt to determine the data bits was to coherently integrate two data lines, where a data bit transition lies between the lines (if a transition lies within a line, the best two lines are chosen). Figure 6 shows a scatterplot of the signal's integrated power, assuming no phase change at the data bit transition points, versus the integrated power, assuming there is a phase change at the transition points, normalized by the highest observed power. The cluster of data points in the lower right represent data bit

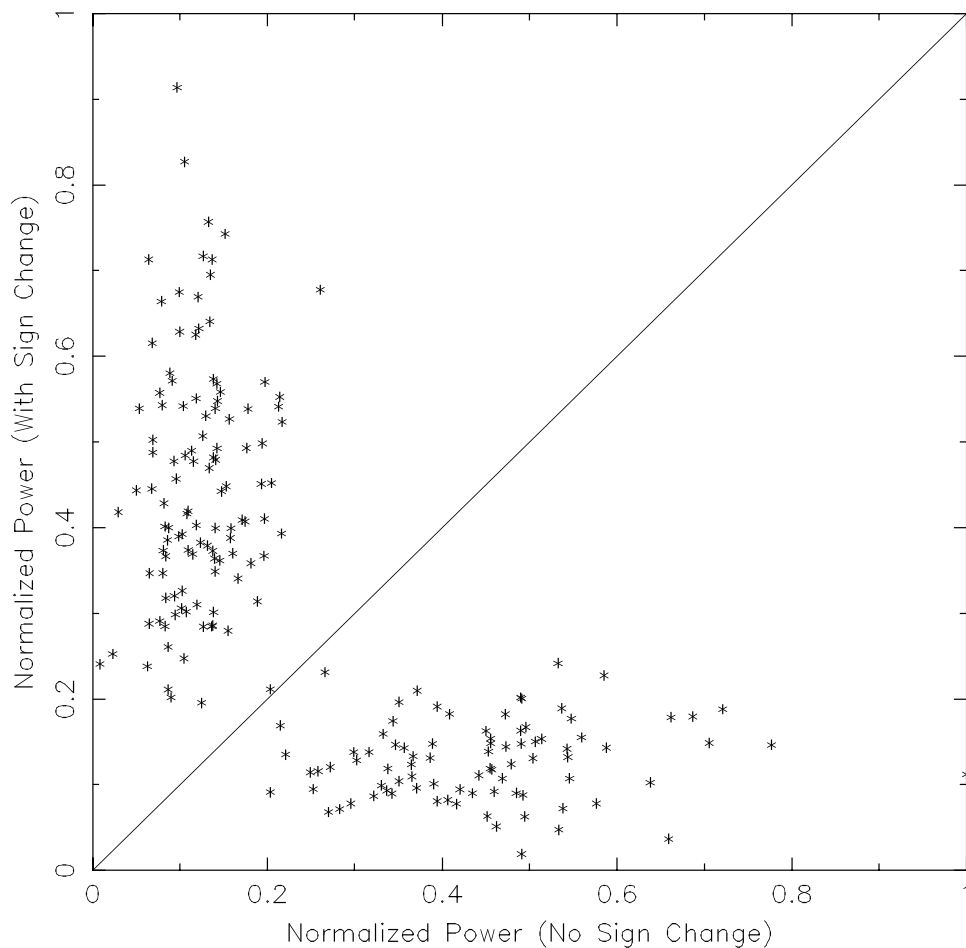


Figure 6. A plot of normalized power assuming that a transition exists between adjacent navigation message bits versus the power and assuming that no transition exists between bits. Each star represents data coherently integrated across a given transition, with the model phase either remaining constant or changing by 180° . The stars near the bottom right are more consistent with no phase change (no data bit sign change), while those in the upper left are more consistent with a 180° phase change (data bit sign change). Points near the diagonal represent data bit transitions that cannot be determined.

transition points that most likely did not have a phase sign change, while those in the upper left did. The data points near the $X = Y$ diagonal, however, represent those data bit transition points where a sign change determination cannot be made. Despite this, by arbitrarily assigning the sign of the first bit and obtaining each successive bit by changing the sign of the previous bit if the corresponding transition point is above the diagonal, or copying it unchanged if it is below the diagonal, a nominal data bit sequence can be determined. The interpretation of this sequence is complicated by the fact that a transition assignment error changes the sign of all following bits. The sequence can be improved by noting the places where the transition was not well determined

(corresponding to data points near the diagonal), including the first arbitrary bit, and modifying them (and thus all following bits) by hand, and comparing to known characteristics of the navigation message. Although the best sequence found in this manner had many recognizable correlations with the expected navigation message, no reliable set of all data bits has been recovered. (For readers familiar with the navigation message, one telemetry word is present having the expected preamble, followed by the expected hand-over word. On the other hand, only one of the six full 30-bit navigation words present passes a parity check.)

[40] Because the data bit transitions cannot be completely determined, and thus represent an unmodeled

phase error, the method used to measure the coherence time completely avoids the transitions by using data well within individual 0.02-s data bits. Modeling is done to account for both breaking the sampled data into navigation data bits and for the effects of the 24% duty cycle and its repetition rate. Each 0.02-s data bit contains about 27.9 data lines. The data in the most central 24 lines within each data bit are used in the following analysis, and the ~ 2 lines on both ends of each bit are rejected. In this way, even large lag correlations cannot be affected by the data bit transitions. To measure the coherence time, the data are coherently integrated over several different time intervals, and the normalized amplitude as a function of lag is formed. Only those integration times that can exactly divide the 24 lines are used. This is equivalent to choosing integration times based on an integer number of lines, for those integers that evenly divide 24. In this way, edge effects are eliminated because the identical data set is used for each coherent integration interval. Figure 7a shows the resulting signals for 1-, 2-, 3-, 4-, 6-, 8-, 12-, and 24-line integrations. The clear decrease in signal amplitude with increasing integration time is completely inconsistent with the direct signal hypothesis but is consistent with a correlation time on the order of a few milliseconds.

[41] To more accurately interpret Figure 7a, a stochastic phase model is used to generate phases with the following property:

$$\langle |\phi(t) - \phi(t + \tau)| \rangle = 1 \text{ rad}, \quad (27)$$

where $\phi(t)$ is the phase in radians at time t and τ is the coherence time. Phases are generated by assuming a random walk process, where the time increments are equal to the sampling time, about 11.1 ns, and phase increments are scaled so (27) is satisfied for a given model τ . For several τ values a large number of 4-s phase time series are generated. These time series are edited to have the same 24% duty cycle as the data and integrated with the same coherence intervals as the data. The resulting simulation amplitudes are averaged and all scaled to the data amplitudes with a one-parameter fit. Figure 7b shows the results. The curves are the simulation amplitudes as a function of integration time, for several coherence times τ . The data points show the data amplitudes for the lag corresponding to the peak in Figure 4a. The data points indicate that the coherence time is about 1.0 ms, which is close to the predicted value and inconsistent with the direct signal prediction, also shown in Figure 7b as a thick curve. It should be noted that the 1.0-ms coherence time value depends on the

definition of coherence, (27) in this case, and is therefore somewhat qualitative. Also, the data points in Figure 7b at the far left of the plot are influenced more by the antenna beam pattern than the coherence properties and thus represent an unmodeled error in this coherence time determination. In fact, as shown in section 4.3, the agreement between the measured coherence time and that expected from the above calculation may be coincidental. Because the measured signal is found to be beam limited, the calculation above should have used the size of the antenna beam rather than the size of the first Y code isorange ellipse. These two sizes just happen to be approximately equal.

[42] For reference, the signal in the 1-s data shows a decrease in SNR with increased integration time, indicating that it is also not a coherent signal on these time-scales. A detailed coherence time measurement was not performed on this signal.

4.3. Antenna Beam Offset From the Specular Direction

[43] The SIR-C antenna was not pointed precisely at the GPS specular reflection point during either the 4-s or 1-s data segments. Using the coordinate system shown in Figure 3b, where the z axis points upward, from the specular reflection point, normal to the ocean's surface, and the x axis is in the incident plane, the shuttle is traveling approximately in the $+y$ direction. Looking at the 4-s and 1-s data, the antenna is pointing approximately at the $x = -5.7$ km, $y = 6.3$ km point, and the $x = -4.7$ km, $y = -34.9$ km point, respectively. The y axis offset of the antenna beam corresponds to a Doppler frequency offset in (18) and can be seen in Figures 8a and 8b to be approximately 510 Hz and -2900 Hz, respectively. Note that the plotted Doppler frequency values are not the absolute Doppler frequencies expected, but are relative to the values expected at the specular point; this also corresponds to the definition of the frequency offset parameter. The Doppler values expected from the peak of the antenna beam are very close to the 497-Hz and -2740 -Hz values observed to maximize the signal SNRs. Introducing these Doppler offsets into the analysis is equivalent to moving the sinc function that appears in (18)'s convolution, in the y direction, and thus optimally overlaps the Doppler and antenna contributions to the integral at the expense of the glistening-zone contribution σ_0^2 , which falls off much more slowly than the antenna gain pattern. In fact, because the frequency maximum for the convolution averages these two competing effects (the glistening

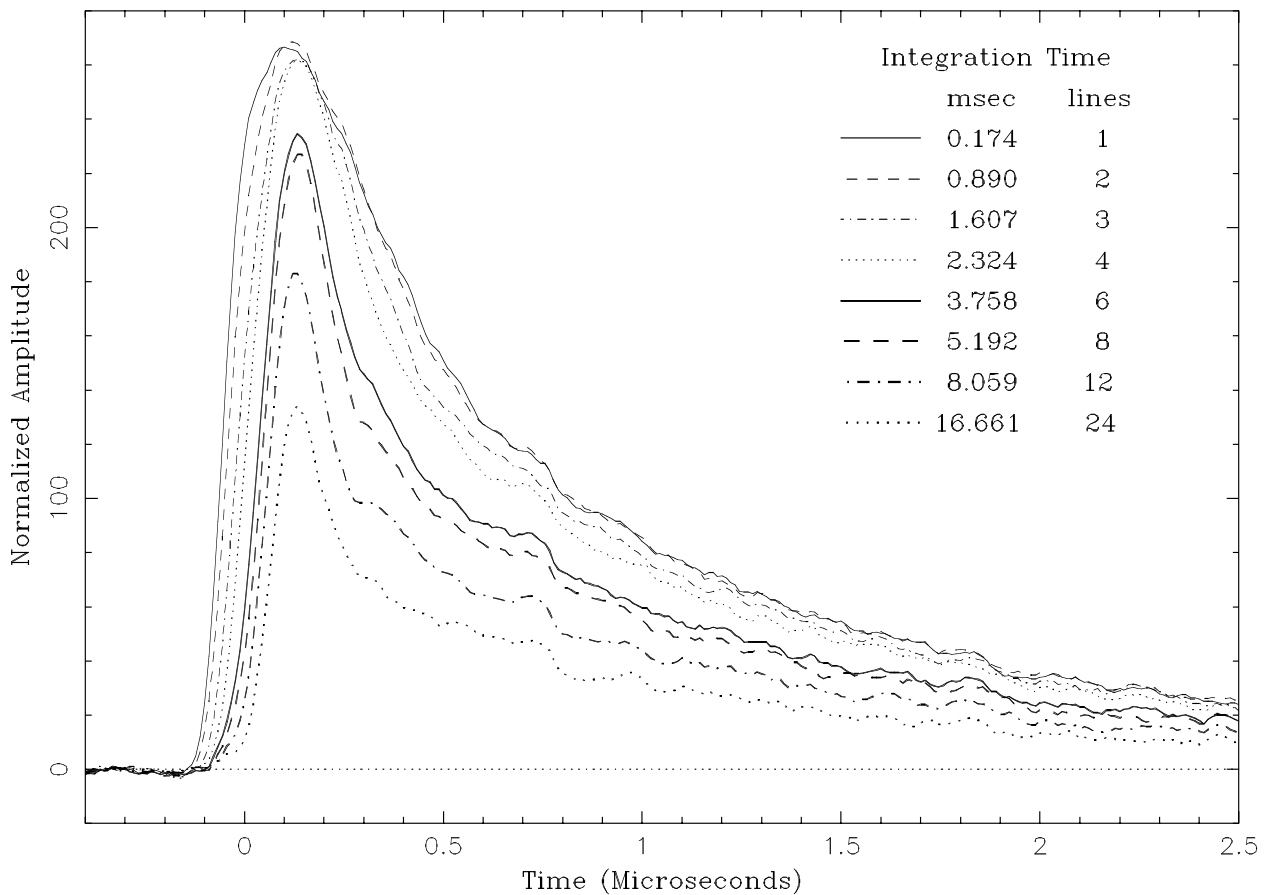


Figure 7a. Signal, using the identical subset of data to avoid the navigation data bit transitions, with different coherent integration times. The number of corresponding data lines, which must evenly divide 24, is also indicated. The peak amplitude falls as the integration interval increases.

zone and the antenna gain pattern), the maximum would be expected to be offset somewhat toward the specular point, or less than the 510-Hz value in the 4-s data, and more than the -2900-Hz value in the 1-s data, as is observed. Compared to the expected direct signal Doppler frequencies, the measured frequency offsets are 690 Hz and -2875 Hz, respectively, too large for any plausible direct signal hypothesis.

4.4. Elimination of Specific Direct Signal Hypotheses

[44] The signal waveform seen in Figure 4a could be caused by a second-order mismodeling effect of the direct signal, where the signal's reception peak over the 4-s data interval forms a parabola in time. Summing such an effect over the 4 s could produce an integrated signal

having a tail similar to that observed (in fact, this was our first working hypothesis when the signal was detected). This effect is shown schematically in Figure 9a, where the integrated signal has an asymmetric tail. If this effect were in our data, it could be seen by plotting the peak reception time as a function of the 4-s data interval. Figure 9b shows this plot, where the maximum amplitude within this range is plotted for each of the 5580 data lines; no curvature is observed.

[45] It could be hypothesized that the waveforms in Figures 4a and 4b are due to multipath delays caused by reflecting surfaces on the shuttle. These figures show that the peak is at least 1 and 4 μ s in width, respectively, and an observable signal persists well beyond these values. These delays correspond to path lengths of 300 m and 1.2 km, respectively. We find no plausible reflection/multipath scenario that can produce observable path delays on

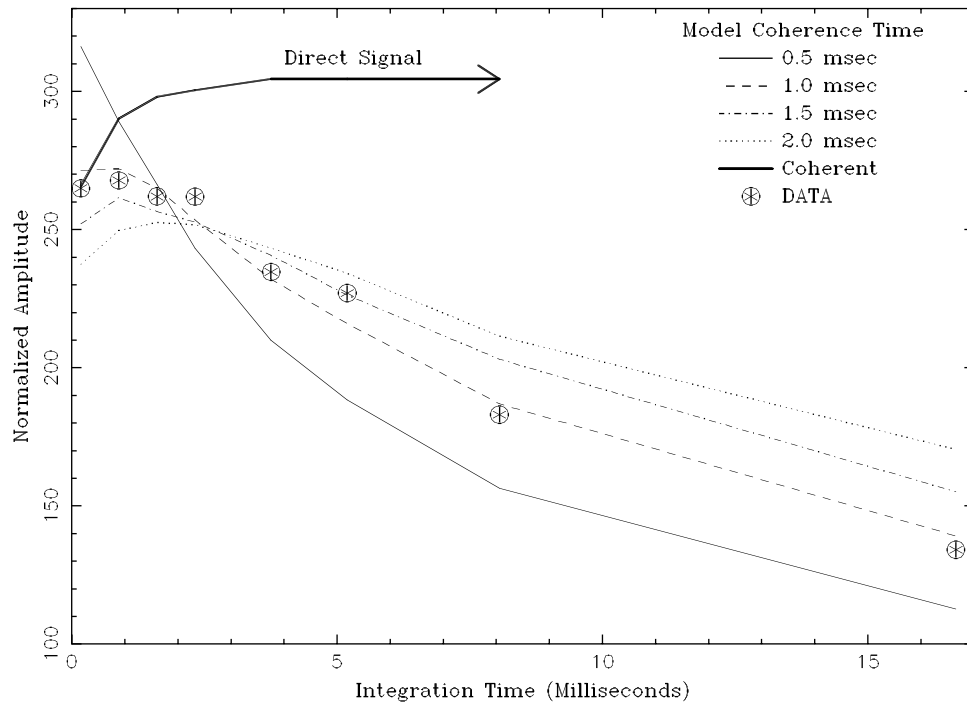


Figure 7b. Normalized amplitude as a function of coherent integration time, as read off Figure 7a (circled stars). The curves show the expected behavior for a variety of coherence times. The circled stars indicate a coherence time around 1.0 ms, consistent with expectations and inconsistent with the expected direct signal behavior, shown with the thick curve.

the order of 1 km using a 40-m by 25-m shuttle, especially considering that the SIR-C antenna was designed to reject off-axis signals.

[46] Because the recording band pass does not fully contain the whole Y code spread spectrum, as shown in Figure 10, it could be hypothesized that cutting the spread spectrum in this way could produce a signal with an asymmetric tail, similar to that observed. This hypothesis has already been implicitly eliminated; the direct signal model waveforms shown in 5a and 5b include the receiver band pass cutting the Y code spectrum. The effect of cutting off this small piece of the Y code spectrum is that the direct signal widens by less than 1% and the amplitude drops about 2%.

5. Future Space-Based Missions

[47] The first spaceborne missions dedicated to GPS reflections will likely perform ocean altimetry and/or wind speed measurements. Such observations must contend with the inherently weak reflected signals which will necessitate a high-gain antenna. Our result is scaled

to determine the expected voltage SNR for a generic altimetry mission and for the SAC-C and CHAMP observations expected soon. This scaling gives the measurement error's system noise component and, thus, helps determine the expected science return. This scaling assumes that the SIR-C ocean conditions and scattering cross section are typical of what would be encountered by these mission scenarios, which may or may not be the case, and the large regional and temporal variations in the ocean's surface state are ignored.

5.1. Scaling to a Generic Altimetry Mission, SAC-C, and CHAMP

[48] To better understand the expected reflection signal SNR from a generic altimetry mission and the resulting altimetry measurement error, we compare the factors involved in scaling the measured SIR-C signal reported here to that of a hypothetical mission orbiting at a height of 400 km, with a 20-, 25-, or 30-dB antenna, using a BlackJack GPS receiver. The BlackJack is NASA's GPS science flight receiver and has been

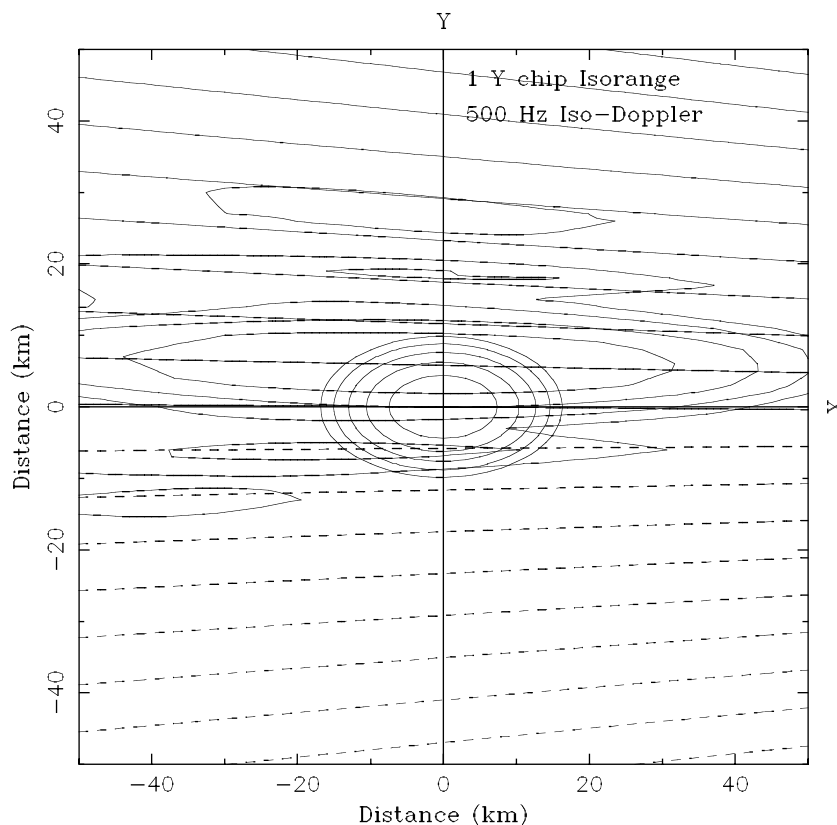


Figure 8a. Plot of the ocean's surface centered on the specular reflection point for the center of the 4-s data epoch. Several isorange ellipses, having 1-Y-code contours, are shown. The iso-Doppler hyperbolas, having 500-Hz contours, are also shown (horizontal curves), where negative Doppler frequency contours are shown as dashed curves. The antenna gain pattern is plotted with 5-dB contours. Notice that the 510-Hz iso-Doppler contour cuts through the approximate center of the antenna beam pattern. This explains the 497-Hz Doppler error parameter that maximizes the signal but cannot be explained by other geometric modeling errors.

delivered, or is scheduled to be delivered, to several missions including the Shuttle Radar Topography Mission (SRTM), SAC-C, CHAMP, Jason-1, Jason-2, Grace, and ICESat. The BlackJack specifications needed for this scaling are that it has a 20.456-MHz sampling rate, utilizes 1-bit samples, and has a 2-ms dead time for each 50-Hz navigation data bit.

[49] Tables 1a–1c present the scaling of the SIR-C result to give the expected signal strength and resulting altimetry error for two signal-processing scenarios: using the public C/A code and using the classified Y code, assuming the code sequence is known. The BlackJack receiver has a Y codeless algorithm that, for high-SNR cases, results in signal SNRs close to that obtained from Y code receivers. For weak signals, like those found

here, processing without the Y code results in a lower SNR than Y code processing. Because a detailed model of the BlackJack algorithm is required to calculate the expected SNR without the Y code, these processing scenarios are not included here.

[50] All entries in the top sections of Tables 1a–1c are in units of decibels, relative to the SIR-C result. The first row of Table 1a notes the loss using the assumed antenna gain versus the SIR-C 38-dB gain, linear-polarized antenna. The SIR-C antenna gain corresponding to the assumed left-handed, circularly polarized reflected signal would be 3 dB less, or 35 dB. The second row deals with the GPS transmitted power levels, relative to the SIR-C L2 Y code (Y2) signal. These numbers do not correspond to the often quoted

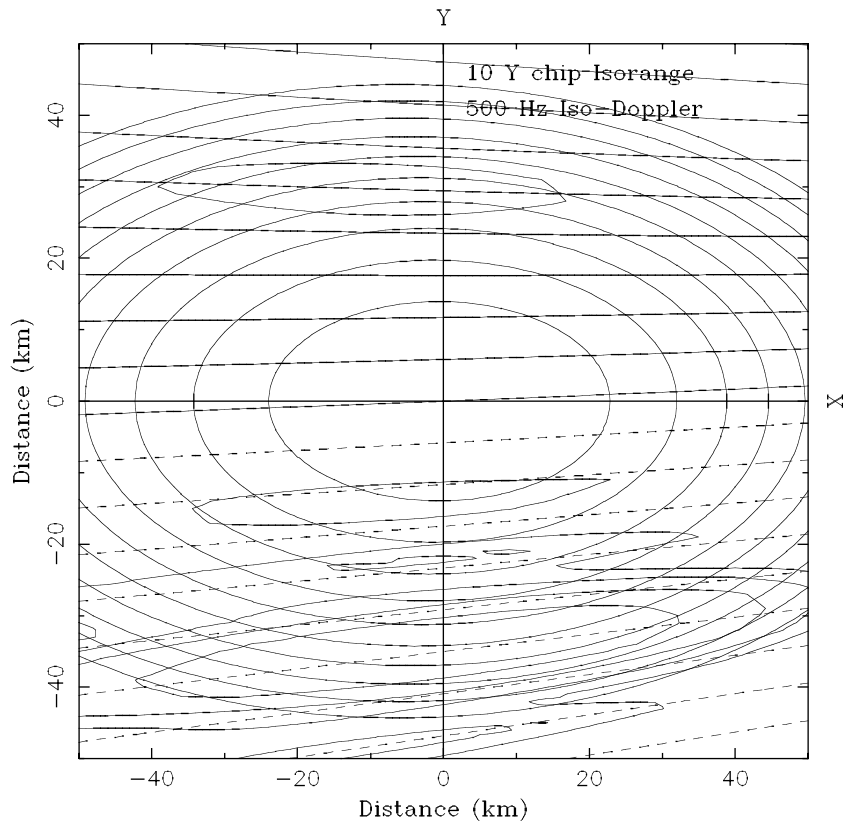


Figure 8b. Plot of the ocean's surface centered on the specular reflection point for the center of the 1-s data epoch. Several isorange ellipses, having 1-Y-code contours are shown. The iso-Doppler hyperbolas, having 500-Hz contours, are also shown (horizontal curves), where negative Doppler frequency contours are shown as dashed curves. The antenna gain pattern is plotted with 5-dB contours. Notice that the -2900 -Hz iso-Doppler contour cuts through the approximate center of the antenna beam pattern. This explains the -2740 Hz Doppler error parameter that maximizes the signal but cannot be explained by other geometric modeling errors.

GPS minimum specifications but are based on the actual measured power levels [Edgar *et al.*, 1998]. The third row accounts for the Blackjack's complex (in-phase and quadrature-phase) recording compared to the SIR-C real data. The fourth row accounts for the 1-bit sampling loss associated with the Blackjack receiver, as compared to the 8-bit sampling used by SIR-C. The fifth row scales the 208-km SIR-C height to the assumed 400-km height of the generic mission. This is done by assuming a 45 incidence angle so that R_r , the distance from the specular point to the receiver, is nominally $400\sqrt{2}$ km for the generic mission, and scaling to SIR-C's corresponding 358-km distance. Finally, the isorange ellipse associated with the C/A code has 10 times the area of the Y code ellipse, which results in approximately 10 times the reflected power

received, as noted in the sixth row of Table 1a. This assumes that the 1-C/A-code isorange ellipse is not limited by either the antenna beam pattern or by the glistening zone, that region of the ocean having probable reflection angles. This entry also account for the assumed elevation angle of 45 compared to the 34 SIR-C elevation angle. For antenna gains greater than about 25 dB the C/A code isorange ellipse will become beam limited, so this entry in Table 1c may be too large. The decibel levels corresponding to the above effects are summed to give the overall expected power decrease relative to the SIR-C result. Note that the SIR-C band pass, which cuts off a small portion of the Y code spread spectrum, is expected to reduce the SNR by about 2%; this small effect is not included in this analysis.

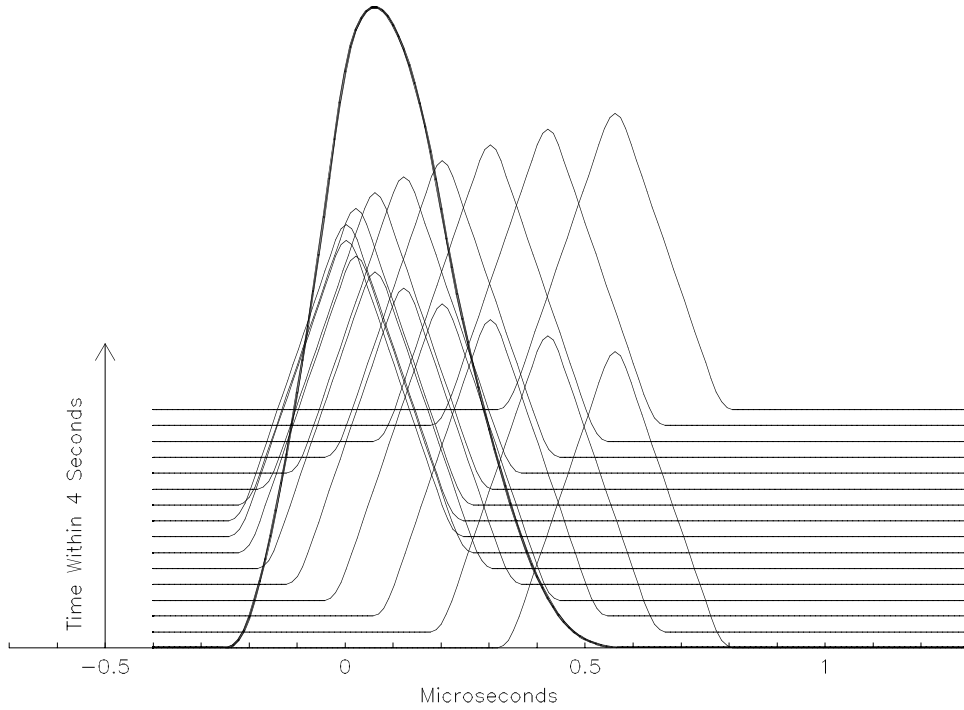


Figure 9a. Schematic plot of hypothetical second-order modeling error that could produce a direct signal tail similar to that seen in the 4-s data. Each peak represents a small portion of the 4 s of data, where the position shifts are parabolic because of second-order mismodeling. The integral of these data over the full 4 s would produce a tail on the right side of the peak.

[51] The lower half of Tables 1a–1c summarizes the steps needed to determine the expected altimetry accuracy. The single-sample voltage SNR R_{ss} is calculated for the SIR-C result by replacing $C(\tau)$ in (24) with nR_{ss}^2 , where n is 15,624, the number of samples in each coherent integration. Using the model described in section 4.1 above, we calculate the expected waveform assuming that the SIR-C antenna was pointed directly at the specular point and calculate a peak SNR of 490. Substituting this expected peak SNR for $S_v(\tau)$ and solving for R_{ss} gives $R_{ss} = 0.0437$. The single-sample SNRs for the generic mission cases are obtained by scaling this result by the total relative decibels given in the upper section of Tables 1a–1c. The 1.6-ms coherence time estimate using (25) and (26) is used rather than the measured value of 1 ms, as the latter is likely corrupted by the beam-limited effects. Substituting the appropriate wavelengths and chip delays into (25) and (26) and assuming $Rr = 400 \sqrt{2}$ km and a 7.0 km s^{-1} velocity results in a C/A code coherence time estimate of 0.33 ms and a Y code coherence time estimate of 1.35 ms. The 1-s voltage SNR, SNR_v , can now be

calculated using (24), where m , the number of integrations, is 1395 for the SIR-C case, and 90% of the inverse of the coherence time in seconds, to account for the BlackJack's 90% duty cycle, for the generic mission case. The number of samples per integration n , defined above, is 15,624 for the SIR-C case and equal to the number of 20.456-MHz samples in a coherence time interval for the generic mission case. The estimated delay error is a function of SNR_v and given by [Thomas, 1995]

$$\begin{aligned}\sigma_\tau(\text{C/A code}) &= \frac{\sqrt{2} \cdot 0.50 \Delta_{\text{C/A}}}{\text{SNR}_v} \sqrt{1 - \rho}, \\ \sigma_\tau(\text{Y code}) &= \frac{\sqrt{2} \cdot 0.37 \Delta_Y}{\text{SNR}_v},\end{aligned}\quad (28)$$

where $\Delta_{\text{C/A}}$ and Δ_Y are the C/A and Y code chip lengths in meters, 293 m and 29.3 m, respectively, ρ is the correlation between samples two lags apart (0.9 in this case), and σ_τ is the delay error in meters. The extra $\sqrt{1 - \rho}$ term in the C/A code formula accounts for the noise cancellation that results from the 20.456-

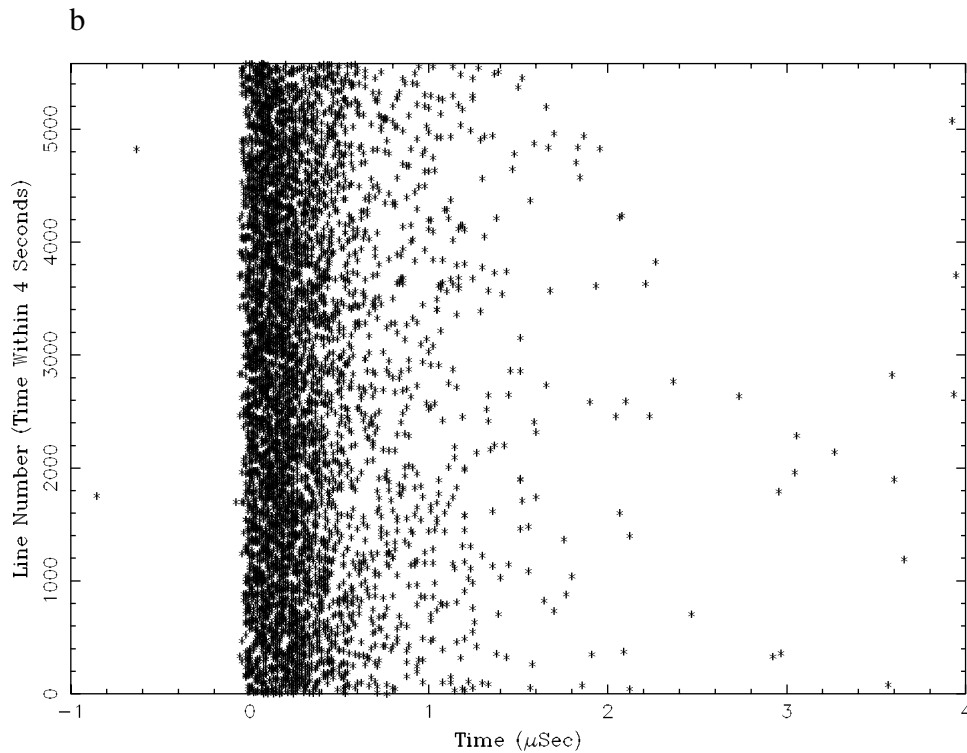


Figure 9b. Plot of peak amplitude for each data line. If an unmodeled second-order mismodeling error caused a tail in the direct signal, as illustrated in Figure 9a, the peak positions in this plot would be parabolic, opening to the right. No evidence of any such mismodeling is seen.

MHz oversampling of the 1.023-MHz chip rate [Thomas, 1995]. Equations (28) are strictly valid for the direct signal only; however, we assume that they are approximately correct for the reflected signal as well. In this case, the error in the difference-of-arrival time between the direct and reflected signals, the primary altimetric observable, is $\sqrt{2}\sigma_\tau$. The altimetric error in this assumed 45° incidence angle geometry is $1/\sqrt{2}$ times the difference-of-arrival time error, or just σ_τ . Thus σ_τ in (28) gives the altimetric error for the geometry assumed here.

[52] Some conclusions can be made concerning altimetry from space-based platforms from the last two rows of Tables 1a–1c. First, the C/A code SNR is expected to be about 5–7 times the Y code (known) SNR because the C/A code’s greater transmission power and factor of 10 greater reflection area more than compensate for the decreased coherence time; for receivers without the Y code, the Y code SNR will be lower yet. On the other hand, even though the Y code altimetry error is somewhat worse than the C/A code error, the much finer spatial resolution available from the smaller Y code isorange ellipse may be more important than the increased SNR.

More measurements, such as those expected soon from SAC-C and CHAMP, and a more detailed model than that presented here are required to better assess the altimetric potential of reflected GPS signals.

[53] Anticipating surface reflection data from the SAC-C and CHAMP Blackjack receivers, Table 2 presents the scaling of this SIR-C result to those missions. The calculations are performed as described above, taking the antenna gains to be 6 dB and 9 dB and the orbit heights to be 750 km and 470 km for SAC-C and CHAMP, respectively. The voltage SNRs listed in the second-to-last line indicate that at least 1 s of data will probably be required to detect signals in SAC-C data; CHAMP data, which will be received at lower altitudes and with a higher-gain antenna, will likely result in higher-quality data. In either case, the scaling model presented here should be greatly improved with these upcoming measurements.

5.2. Wind Speed Determination

[54] Future space-based missions using a highly directional antenna will have the signal shape and dynamic range dominated by the antenna pattern (antenna-beam-

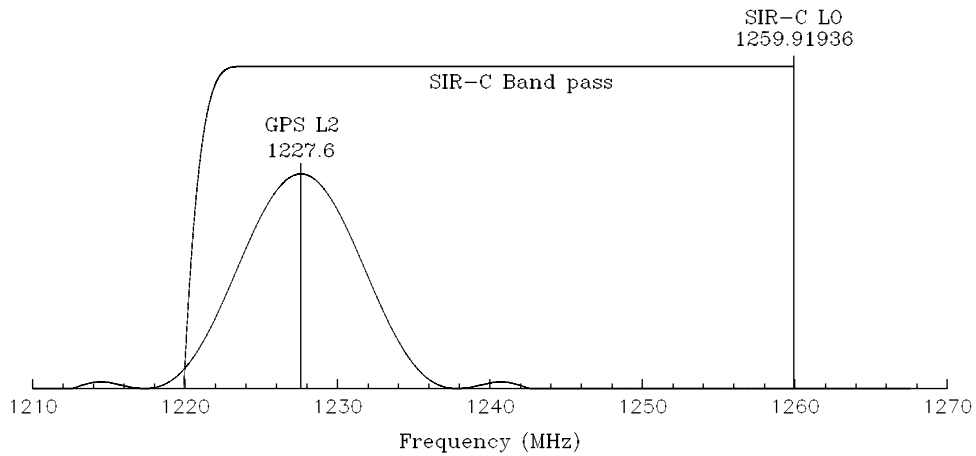


Figure 10. SIR-C recording spectrum and the Y code spread spectrum from GPS 39.

limited footprint), so a change in wind speed will produce a change in the signal's peak value, while the leading and the trailing edges will be basically unchanged. This situation is rather different from that of a receiver at a low altitude when a broad-beamed antenna is used (isorange-limited footprint), such as reported by *Garrison et al.* [1998] or *Komjathy et al.* [2000], where the slope of the signal's trailing edge is dependent on the wind speed. Therefore it will be very important to understand all systematic effects affecting amplitude, and some form of amplitude calibration will likely be required.

[55] In the analysis presented in this paper, c_0 in (18) was chosen arbitrarily so that the model and the 4-s data had approximately the same peak SNR. If c_0 is chosen on the

basis of expected GPS L2 signal transmission power and realistic system temperatures, a wind speed can be determined which gives the best fit to the data. Figure 11 shows the expected signal for various wind speeds. Comparing these curves with the measured peak SNR of 334 results in a wind speed of 4.3 m s^{-1} , consistent with speeds measured near the Galapagos Island at the time these data were collected, but this value should be interpreted as a qualitative estimate only, given the large uncertainties in many of the parameters used to obtain this number.

6. Summary and Conclusions

[56] The signals shown in Figures 4a and 4b are the first measurements of an Earth-reflected GPS signal observed

Table 1a. Comparison of This Paper's SIR-C Result With a Generic Altimetry Mission Having a 20-dB Gain Antenna and Using the C/A or Y Code Signals and Summary of the Steps in the Expected 1-s Voltage SNR and Altimetry Error Calculations

	SIR-C (L2) Y2 Code Known	Generic 20-dB Mission (L1)	
		C/A Code	Y1 Code Known
Receiving antenna gain ^a	0	-15.0	-15.0
Transmission power ^a	0	4.0	1.0
Complex sampling ^a	0	3.0	3.0
Sample quantization ^a	0	-2.0	-2.0
Receiver height ^a	0	-4.0	-4.0
Reflection area ^a	0	11.9	1.9
Total ^a	0	-2.0	-15.0
Single-sample SNR _V	0.0437	0.0346	0.0077
Coherence time, ms	1.56	0.52	2.12
Expected SNR _V (1 s)	245	156	22
Altimetry error, m	0.06	0.42	0.69

^a Given in relative decibels.

Table 1b. Same as Table 1a, Except a 25-dB Gain Antenna is Assumed

	SIR-C (L2)Y2 Code Known	Generic 25-dB Mission (L1)	
		C/A Code	Y1 Code Known
Receiving antenna gain ^a	0	-10.0	-10.0
Other effects in Table 1a ^a	0	13.0	0.0
Total ^a	0	3.0	-10.0
Single-sample SNR _r	0.0437	0.0615	0.0138
Coherence time, ms	1.56	0.52	2.12
Expected SNR _r (1 s)	245	328	56
Altimetry Error, m	0.06	0.20	0.27

^a Given in relative decibels.

form a space-based platform. These signals' temporal shape, coherence properties, and reception frequencies agree closely with those expected for a reflected GPS signal, but do not agree with direct signal models. Designers of future space-based GPS reflection missions can scale this measurement to determine the expected SNR and hence an estimate of the altimetry accuracy.

[57] It should be noted that this analysis, and specifically the large number of lag calculations, could not have been performed without the raw, 90-MHz-sampled data available from the SIR-C archives. The ability to calculate with arbitrary phase/Doppler models was also extremely useful. Follow-on work by the authors and their collaborators in the area of GPS reflection altimetry and scatterometry, using lower altitudes platforms, has retained this flexibility by recording and analyzing the raw, 20-MHz-sampled GPS signals available from many types of GPS receiver front ends. This work has led to the development of a second-generation receiver

system for GPS reflections remote sensing [Lowe *et al.*, 2002] that records the high-rate data and processes them with a software receiver. The ability to use raw, sampled data for a variety of analyses, and to reprocess the data numerous times with different software receiver configurations, more than compensates for the additional processing required, especially in the research and development phase of this technology development.

Appendix A: Using Fourier Transforms to Speed Up Lag Calculations

[58] The material presented here may be familiar to some readers but is included for completeness. The convolution theorem states that the Fourier transform of a convolution of two functions is the product of the transforms of the two functions [Bracewell, 1965]. The modified form used here states that in the discrete

Table 1c. Same as Table 1a, Except a 30-dB Gain Antenna is Assumed

	SIR-C (L2) Y2 Code Known	Generic 30-dB Mission (L1)	
		C/A Code	Y1 Code Known
Receiving antenna gain ^a	0	-5.0	-5.0
Other effects in Table 1a ^a	0	13.0	0.0
Total ^a	0	8.0	-5.0
Single-sample SNR _r	0.0437	0.1094	0.0245
Coherence time, ms	1.56	0.52	2.12
Expected SNR _r (1 s)	245	640	124
Altimetry Error, m	0.06	0.10	0.12

^a Given in relative decibels.

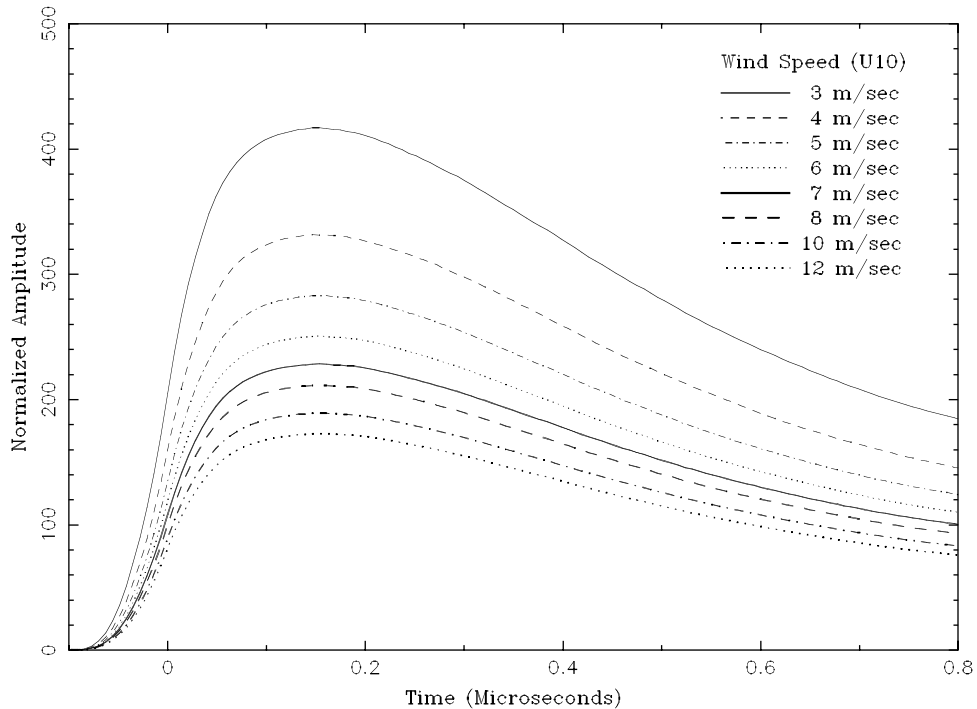
Table 2. Comparison of This Paper's SIR-C Result With a SAC-C and CHAMP Missions, Assuming the C/A Code Is Used, and Summary of the Steps in the Expected 1-s Voltage SNR and Altimetry Error Calculations

	SIR-C (L2)Y2 Code Known	SAC-C C/A Code	CHAMP C/A Code
Receiving antenna gain ^a	0	-29.0	-26.0
Transmission power ^a	0	4.0	4.0
Complex sampling ^a	0	3.0	3.0
Sample quantization ^a	0	-2.0	-2.0
Receiver height ^a	0	-9.4	-5.4
Reflection area ^a	0	14.6	12.6
Total ^a	0	-18.8	-13.7
Single-sample SNR _V	0.0437	0.0050	0.0090
Coherence time, ms	1.56	0.72	0.57
Expected SNR _V (1 s)	245	6.0	16.8
Altimetry error, m	0.06	11	3.9

^a Given in relative decibels.

case the inverse Fourier transform of a correlation is the product of one function's inverse transform with the inverse transform of the other function in reverse order (other than the first sample). Thus, to calculate (15) quickly, we form the inverse FFT of the data and

the inverse FFT of the model's complex conjugate, where the model values, other than the first, are in reverse order. The FFT of the product of these two transforms will give S_I . This can be shown explicitly by writing the inverse Fourier transform (FT) of the N data

**Figure 11.** Expected normalized amplitude (voltage SNR) for different wind speeds, as described in the text. This shows qualitatively how the SNR changes with wind speed; the curves have essentially the same shape and differ by an overall scale factor.

samples, δ_j :

$$\delta_j = \sum_{k=0}^{N-1} D_k e^{2\pi i(kj/N)} \quad j, k = 0, 1, \dots, N-1. \quad (A1)$$

The model complex conjugate values M_l^* are reversed and inverse fast Fourier transformed:

$$\mu_j = \sum_{m=0}^{N-1} \mathbf{M}_{N-m}^* e^{2\pi i(mj/N)} \quad j, m = 0, 1, \dots, N-1, \quad (A2)$$

where μ_j is the inverse FT of the reversed model. The FT of the product, S_l , can be written

$$\begin{aligned} S_l &= \frac{1}{N} \sum_{j=0}^{N-1} \delta_j \mu_j e^{-2\pi i(lj/N)} \\ &= \frac{1}{N} \sum_{m=0}^{N-1} \sum_{k=0}^{N-1} D_k \mathbf{M}_{N-m}^* \sum_{j=0}^{N-1} e^{(2\pi i/N)(k+m-l)j} \\ &= \frac{1}{N} \sum_{m=0}^{N-1} \sum_{k=0}^{N-1} D_k \mathbf{M}_{N-m}^* N \delta(k+m-l) \\ &= \sum_{k=0}^{N-1} D_k \mathbf{M}_{k-l}^*, \end{aligned} \quad (A3)$$

which is exactly (15), thus proving that this FFT technique provides the identical result as the explicit calculation.

[59] **Acknowledgments.** The research described in this paper was carried out by the Jet Propulsion Laboratory, California Institute of Technology, under contract with the National Aeronautics and Space Administration. Funding for this study was provided by NASA's Solid Earth and Natural Hazards Program, NASA's Instrument Incubator Program, and NASA's Physical Oceanography Program. We wish to thank David Perz and Brian Swift (JPL) for providing the raw SIR-C data, Scott Shaffer (JPL) for providing the SIR-C antenna beam pattern model, and Peter Briggs and Darren Graham (DERA) for providing the Y code.

References

- Bass F. G., and I. M. Fuks, *Wave Scattering From Statistically Rough Surfaces*, Pergamon, New York, 1979.
- Bracewell, R. N., *The Fourier Transform and Its Applications*, McGraw-Hill, New York, 1965.
- Brown, G. S., The average impulse response of a rough surface and its applications, *IEEE Trans. Antennas Propag.*, AP-25, 67–74, 1977.
- Defense Mapping Agency, World Geodetic System 1984 (WGS-84): Its definition and relationships with local geodetic system, *DMA TR 8350.2*, 2nd ed., Fairfax, Va., 1984.
- Edgar, C., J. Price, and D. Reigh, GPS Block IIA and IIR received signal power measurements, in *Proceedings of the National Technical Meeting "Navigation 2000,"* pp. 401–412, Inst. of Navig., Alexandria, Va., 1998.
- Elfouhaily, T., B. Chapron, K. Katsaros, and D. Vandemark, A unified directional spectrum for long and short wind-driven waves, *J. Geophys. Res.*, 102, 15,781–15,796, 1997.
- Garrison, J. L., Airborne reflected GPS experiments: Higher altitudes and rougher seas, paper presented at GPS Applications to the Structure and Dynamics of the Earth's Oceans and Ionosphere Workshop, NASA, Arcadia, Calif., 1–3 Dec. 1998.
- Garrison, J. L., S. J. Katzberg, and M. I. Hill, Effect of sea roughness on bistatically scattered range signals from the Global Positioning System, *Geophys. Res. Lett.*, 25, 2257–2260, 1998.
- Katzberg, S., Application of GPS altimetry for Wetlands mapping, paper presented at GPS Applications to the Structure and Dynamics of the Earth's Oceans and Ionosphere Workshop, NASA, Arcadia, Calif., 1–3 Dec. 1998.
- Klein, L. A., and C. T. Swift, An improved model for the dielectric constant of sea water at microwave frequencies, *IEEE Trans. Antennas Propag.*, AP-25, 104–111, 1977.
- Komjathy, A., V. Zavorotny, P. Axelrad, G. Born, and J. Garrison, GPS signal scattering from sea surface: Wind speed retrieval using experimental data and theoretical model, *Remote Sens. Environ.*, 73(2), 162–174, 2000.
- Lowe, S., Voltage SNR nonlinearity resulting from incoherent summations, *TMO Progress Rep. 42-137*, Jet Propul. Lab., Pasadena, Calif., May 1999. (Available at http://tmo.jpl.nasa.gov/tmo/progress_report).
- Lowe, S., J. LaBrecque, L. Young, and J. Lerma, GPS reflections: JPL aircraft experiments, paper presented at GPS Application to the Structure and Dynamics of the Earth's Oceans and Ionosphere Workshop, NASA, Arcadia, Calif., 1–3 Dec. 1998.
- Lowe, S. T., P. M. Kroger, G. W. Franklin, J. L. LaBrecque, J. Lerma, M. F. Lough, M. R. Marcin, D. J. Spitzmesser, and L. E. Young, A delay/Doppler-mapping receiver system for GPS-reflection remote sensing, *IEEE Trans. Geosci. Remote Sens.*, in press, 2002.
- Martin-Neira, M., A passive reflectometry and interferometry system (PARIS): Application to ocean altimetry, *ESA J.*, 17, 331–335, 1993.
- Martin-Neira, M., M. Caparrini, J. Font-Rossello, S. Lannelongue, and C. S. Vallmitjana, The PARIS concept: An Experimental demonstration of sea surface altimetry using GPS reflected signals, *IEEE Trans. Geosci. Remote Sens.*, 39(1), 142–150, 2001.
- Rockwell STSOC, Internal ICD PATH Product, *ICD-I-TOP-002A (JSC-18645)*, Johnson Space Cent., Houston, Tex., 27 May 1992.
- Rockwell STSOC, Internal ICD PATH Product, *ICD-I-TOP-*

- 002C, Johnson Space Cent., Houston, Tex., 11 June 1997.
- Spilker, J. J., Signal structure and performance characteristics, *Navigation*, 1, 29–54, 1980.
- Stratton, J. A., *Electromagnetic Theory*, McGraw-Hill, New York, 1941.
- Thomas, J. B., Signal-processing theory for the TurboRogue receiver, *JPL Publ.*, 95-6, 1995.
- Ulaby, F. T., R. K. Moore, and A. K. Fung, *Microwave Remote Sensing, Active and Passive*, Artech House, Norwood, Mass., 1982.
- Zavorotny, V. U., and A. G. Voronovich, Scattering of GPS signals from the ocean with wind remote sensing application, *IEEE Trans. Geosci. Remote Sens.*, 38(2), 951–964, 2000.
-
- G. A. Hajj, S. T. Lowe, L. J. Romans, L. E. Young, and C. Zuffada, Jet Propulsion Laboratory, California Institute of Technology, 4800 Oak Grove Drive, Pasadena, CA 91109, USA. (george.a.hajj@jpl.nasa.gov; stephen.t.lowe@jpl.nasa.gov; larry.j.romans@jpl.nasa.gov; lawrence.e.young@jpl.nasa.gov; cinzia.zuffada@jpl.nasa.gov)
- J. L. LaBrecque NASA, 300 E Street, S. W., Washington, D. C., 20546-0001, USA. (jlabrecq@hq.nasa.gov)